Università degli Studi di Napoli *Federico II*

DOTTORATO DI RICERCA IN

FISICA FONDAMENTALE ED APPLICATA

Ciclo: XXVI

Coordinatore: prof. Raffaele Velotta

Study of a Multivariate Technique for the Search of Single Top-Quark Production with $\sqrt{s} = 8$ TeV in the CMS Experiment at CERN

Settore Scientifico Disciplinare FIS/05

Dottorando

Oktay Doğangün

Tutore

Dr. Luca Lista

Dr. Mario Merola

Anni 2011/2015

Contents

Contents iii

Introduction 1

I The Theory: Standard Model and Top Quark 5
- I.1 The Standard Model . . . 6
  - I.1.1 Quantum Electrodynamics . . . 8
  - I.1.2 Electroweak Inteactions and the Higgs Mechanism . . . 11
  - I.1.3 Strong Interactions . . . 16
- I.2 Top Quark . . . 17
  - I.2.1 Decays . . . 19
  - I.2.2 Top Quark Production . . . 20
  - I.2.3 Experimental Results . . . 23

II The Experiment: LHC and CMS 25
- II.1 The Large Hadron Collider . . . 26
  - II.1.1 Design and Layout . . . 28
  - II.1.2 Magnets . . . 29
  - II.1.3 Vacuum System . . . 30
  - II.1.4 RF Acceleration System . . . 31
  - II.1.5 Accelerator Physics . . . 31
- II.2 The Compact Muon Selenoid . . . 33
  - II.2.1 Detector Design . . . 33
  - II.2.2 Superconducting Magnets . . . 33
  - II.2.3 Tracking System . . . 34
  - II.2.4 Electromagnetic Calorimeter . . . 35
  - II.2.5 Hadron Calorimeter . . . 36
  - II.2.6 Forward Detectors . . . 37
  - II.2.7 Muon System . . . 37
  - II.2.8 Trigger . . . 38
- II.3 Reconstruction . . . 39
  - II.3.1 Particle Flow Algorithm . . . 39
  - II.3.2 Tracking Charged Particles . . . 40
  - II.3.3 Electrons . . . 41
  - II.3.4 Muons . . . 41
  - II.3.5 Jet Algorithm . . . 43

II.3.6 Missing Energy 44

III The Analysis: Single Top-Quark Cross-Section Measurement using Multivariate Techniques 45

III.1 Event Selection and Reconstruction 46
III.1.1 Primary Vertex, Noise Cleaning and Triggers 47
III.1.2 Electrons and Muons 47
III.1.3 Jets 48
III.1.4 Missing transverse energy and W-boson transverse mass 49
III.1.5 b-tagging and mistagging 50
III.1.6 Top quark 51
III.2 Control Samples and Data-driven Background Estimations 52
III.2.1 Vector Bosons + jets 52
III.2.2 Top-antitop 52
III.2.3 QCD Background Estimation 53
III.3 Systematic Uncertainties 53
III.3.1 Background Normalisation 54
III.3.2 Instrumental Uncertainties 54
III.3.3 Theoretical Uncertainties 55
III.4 BDT Discriminant 55
III.4.1 Determining Variables 57
III.4.2 Training and Testing 66
III.4.3 Fit Procedure and the Measurement 69
III.5 Results 73

Conclusion 75

Acknowledgements 76

List of Figures 77

List of Tables 79

Bibliography 81

Introduction

There are two main approaches so far in the human history to understand the nature: reductionism and holism. In a reductionist view, the universe is understood in terms of its pieces, while in the holistic picture, the pieces are understood in terms of the universe itself.

Physics has been using the two approaches in every part of any research. However, one could roughly consider that the physics is actually divided into these points of view in terms of the theories so far, namely the Standard Model of Particle Physics, describing the universe by reducing everything to particles, and the Standard Model of Cosmology, considering the effects of the whole universe on a body of interest.

The physicists have failed to find a theory that describes both the particle physics and the cosmology so far. However, as the experiments and theoretical tools get advanced, the two descriptions would meet at a point where as well as the two approaches start to combine.

This work is presenting a study for the search of the single top-quark production in the CMS Experiment at CERN focusing on the s-channel process and muon decay mode as the final state topology, using a multivariate technique based on the Boosted Decision Trees (BDT) algorithm. The multivariate technique is utilized with an optimization procedure for understanding what are the appropriate variables to use for separation of the signal and background events.

The particle in interest for this analysis, known as top quark, is the heaviest elementary particle predicted by the Standard Model and discovered so far, even heavier than the Higgs boson, discovered in 2012, which itself gives mass to the top quark. It has been discovered after a long survey beginning from the prediction in 1974 by Christenson *et al.* to the discovery announcement by CDF and DØ in 1994.

Top quark was first postulated in order to dismiss the complications in the established theoretical model of hadrons due to the observation of CP-Violations in kaon decay, followed by Kobayashi and Maskawa who suggested a third generation of quarks to rectify theory and experiment. The additional doublet was called “top” and “bottom” in the spirit of “up” and “down” quarks by Harari who echoed the prediction of a new generation of quarks.

Top quark gives the unique opportunity to perform a direct measurement of the element of the quark-mixing matrix involving the b quark, which is one of the Standard Model parameters. The prompt decay of top quark due to its heavy mass reveals the possibility to investigate the properties of a bare quark before forming any bound state, unlike other quarks known so far.

Beside its importance to the Standard Model, top quark also provides a window for a possible new physics beyond the Standard Model, such as an extra intermediate charged boson W', fourth generation quarks, charged Higgs boson.

This work is structured in three main chapters:

Chapter I The Theory. The first chapter is presenting the theoretical framework of the top quark physics starting from the Standard Model of particle physics. After introducing Quantum Electrodynamics, the electroweak and strong interactions are constructed as an extension of it in a gauge-theoretical manner. Then in the following section, the top quark is detailed considering its decay and its two production mechanisms, together with the windows it opens for the feature physics beyond the Standard Model.

Chapter II The Experiment. The second chapter is illustrating the experimental setup detailing the accelerator complex and the detector together with some phenomenological concepts on collider physics. The first section of the second chapter introduces the accelerator complex, the Large Hadron Collider (LHC), while the second section gives a detailed description of the Compact Muon Selenoid (CMS) detector where the data is taken. The third section is about the concepts and physical aspects that the physicists deal with, in the collider phenomenology.

Chapter III The Analysis. The analysis reported in the third chapter is on the collision data collected at 8 TeV in the CMS detector with a luminosity of 19.3 fb^{-1}, focused on muonic decay of the top quark in the s-channel topology. The first section of this chapter is about the event selection used in the analysis while in the second section, the control samples and backgrounds are explained. The third section is about the systematic uncertainties. The fourth section gives a detailed explaination of the analysis using a multivariate technique called the Boosted Decision Trees (BDT) by choosing the most discriminating variables via a feedback loop. The results of the analysis are given in the last section.

Chapter I

The Theory: Standard Model and Top Quark

Theories in particle physics are formulated as relativistic field theories where the fundamental entities are fields as a function of space-time, and particles are described as oscillations of these fields. In a subset of field theories the interactions are modeled in terms of an exchange of force carrying fields imposing some symmetries in the theory, called gauge symmetries.

A field theory is described in terms of actions which are functionals of a Lagrangian and can be variated to derive the equations of motions for various fields of the model in subject.

$$S\left[\phi_i(x)\right] \;=\; \int d^4x\, \mathcal{L}\left(\phi_i(x)\right)$$

where $\mathcal{L}$ is the Lagrangian density as a function of the fields $\phi_i(x)$ and their space-time derivatives.

A gauge symmetry corresponds to that the laws of physics do not change under some phase change of the fields, requiring an invariance of the form of the Lagrangian under a group of transformations. These transformations form a set that has some basic algebraic properties, i.e., associativity, inversability and having a unit element. The groups having commutativity are called Abelian which physically corresponds to self-interacting gauge fields.

Throughout this chapter, it is used the natural units, namely the convension $\hbar \equiv c \equiv 1$ where $\hbar = 6.6 \times 10^{-25}$GeV-s is the reduced Planck constant, $c = 3.0 \times 10^{8}$m/s is the speed of light and GeV is giga electron volts[1]. Therefore, the fundamental units can be read as follows, in terms of proton mass which is approximately 1 GeV:

$$1\text{m} = 1.5 \times 10^{16}\text{GeV}^{-1}\,, \qquad 1\text{s} = 4.5 \times 10^{24}\text{GeV}^{-1}\,, \qquad 1\text{kg} = 0.5 \times 10^{27}\text{GeV}$$

This chapter gives a brief introduction to the Standard Model of Particle Physics in terms of fundamental interactions, followed by a detailed section dedicated for the top-quark part of the Standard Model in a phenomenological point of view. Experimental evidence of the Standard Model is given very shortly while recent researches aboout the top quark is listed in the end of the chapter.

I.1 The Standard Model

The Standard Model of Particle Physics is a parametrization of the Quantum Field Theory where the particles are quantizations of fields interacting according to an algebraic group. More precisely, Standard Model consists of three types of interactions of nature, namely electromagnetic, weak and strong interactions, which are unifiable in the base of the parameters subject to the experiments [2–6].

Each interaction in this picture is described by a symmetry that give rise to a conservation of a quantity in and out of that interaction. These symmetries are well understood by some transformations that form an algebraic group, called the gauge group, while the conserved quantity, namely the physical charge, is simply the generator of that group [7, 8]. So, the Standard Model is a product of three gauge groups, each corresponds to an interaction, as follows:

$$\underbrace{\mathrm{U}(1)_Y}_{\text{hypercharge}} \otimes \underbrace{\mathrm{SU}(2)_L}_{\text{isospin}} \otimes \underbrace{\mathrm{SU}(3)_C}_{\text{color charge}}$$

where $\otimes$ is group product, $\mathrm{U}(1)_Y$ is the Unitary Group of the hypercharge Y, $\mathrm{SU}(2)_L$ is the Special Unitary Group of the isospin $\vec{T}$, and $\mathrm{SU}(3)_C$ is the Special Unitary Group of color charge λ. Each group has a fundamental representation which corresponds to

[1] 1 electron volt is the energy needed for an electron to travel 1 meter under an electrical potential of 1 volt [1].

the particles of the matter like electron or neutrino, and an adjoint representation which corresponds to the force-carrying particles like photon or nuclear force.

The first two symmetries break down simultaneously via the Higgs mechanism [9–12] into a unitary symmetry of the electric charge, Q which is related to the z component of the isospin charge and the hypercharge by the Gell-Mann–Nishijima formula:

$$\begin{array}{ccccc} \mathrm{U}(1)_Y & \otimes & \mathrm{SU}(2)_L & \rightsquigarrow & \mathrm{U}(1)_Q + \text{massive bosons} \\ \frac{1}{2}Y & + & T^3 & = & Q \end{array}$$

After the breakdown, the three gauge bosons of the former groups are eliminated via field redefinitions by the three states of the Higgs field to form massive gauge bosons responsible for the weak nuclear forces, namely the W bosons and the Z boson, so that a massless photon responsible for the electromagnetic force remains and a chargeless Higgs boson becomes observable. The isospin and hypercharge symmetries are indeed broken due to the precence of the masses of the W and Z bosons while the new symmetry of the electrical charge is not since the photon remains completely massless.

The Standard Model predicts three generation of fermions which consist of two main categories called quarks and leptons (Table I.1). There does not exist a fundamental interaction between quarks and leptons since the color symmetry of $\mathrm{SU}(3)_C$ is not broken and leptons are color-singlets while quarks have three types of color charge, so-called "red", "green" and "blue" [2].

Each fermion has a left-hand and a right-hand helicity, which is defined simply by the contrast between the directions of its spin and the velocity vectors, each having different quantum numbers. Both quarks and leptons form one isospin doublet and two singlet states for each generation. Each isospin doublet has $T = +1$ and $Q = -1$ in total so that it can interact with $W^{\pm}$ and Z bosons while singlets can not. Especially, the right-hand neutrino singlets, ν_R^i, are completely isolated (or do not even exist) according to the Standard Model, so they do not have any kind of charge. This means that the weak interaction simply breaks the left-right symmetry.

The photon and Z boson are a combination of two parts, each stemming from the isospin group and the hypercharge group, with a mixture angle called the weak angle, θ_w, which is just in the exact value that makes the mass of the photon exactly zero, i.e., $M_\gamma = 0$.

[2] The color charge has nothing to do with physical colors. The names are given so just because there exist three types of conserved quantity for the group SU(3).

Fields		Generations			Color	T_3	Q
Quarks	Q_L^i	$\begin{pmatrix} u_L \\ d_L \end{pmatrix}$	$\begin{pmatrix} c_L \\ s_L \end{pmatrix}$	$\begin{pmatrix} t_L \\ b_L \end{pmatrix}$	**3**	$+1/2$ $-1/2$	$+2/3$ $-1/3$
	u_R^i	u_R	c_R	t_R	**3**	0	$+2/3$
	d_R^i	d_R	s_R	b_R	**3**	0	$-1/3$
Leptons	L_L^i	$\begin{pmatrix} \nu_{eL} \\ e_L \end{pmatrix}$	$\begin{pmatrix} \nu_{\mu L} \\ \mu_L \end{pmatrix}$	$\begin{pmatrix} \nu_{\tau L} \\ \tau_L \end{pmatrix}$	**1**	$+1/2$ $-1/2$	0 -1
	e_R^i	e_R	μ_R	τ_R	**1**	0	-1
	ν_R^i	ν_{eR}	$\nu_{\mu R}$	$\nu_{\tau R}$	**1**	0	0
Higgs	H		$\begin{pmatrix} \phi^+ \\ \phi^0 \end{pmatrix}$		**1**	$+1/2$ $-1/2$	$+1$ 0
Vectors	W		W^+		**1**	$+1$	$+1$
	Z		Z		**1**	0	0
	γ		A		**1**	0	0
	G		G		**8**	0	0

TABLE I.1: The periodic table of Standard Model. The anti-particles are not included.

Therefore, this parameter of the Standard Model importantly gives the ratio between the mass of the W and Z boson, as follows:

$$\cos\theta_w = \frac{M_W}{M_Z} \tag{I.1}$$

where it corresponds to $\sin^2\theta_w \approx 1/4$.

The gluons, G, have eight colors which are a combination of a color and an "anti-color", so that quarks could interact with the gluons to change their color but not their flavours, isospins or electric charges. The gluons are presumed to be massless since it is not a broken symmetry.

I.1.1 Quantum Electrodynamics

Quantum Electrodynamics (QED), the theory describing the interactions between light and matter, is the first true and successful quantum field theory that was developed [13–17]. All further theories are an extention of the theory to a more general gauge group. Namely, it is the most simple case of a gauge group: the Abelian case, which means that it has no self-interacting terms for the photon as what is observed indeed.

QED is the first theory which describes the force as a particle exchange, by explaining the four-fermion interaction of the Fermi theory as a virtual photon exchange between

electrons or positrons. The photons are called virtual because they are observed indirectly as a momentum transfer.

The strength of the interaction is precisely given by taking into account high order interactions which is the case in the real world, namely as fine structure constant $\alpha_{\rm e} \equiv {\rm e}^2/4\pi \approx 1/137$ is measured to be

$$\alpha_{\rm e} \quad = \quad 7.297\,352\,5698(24) \times 10^{-3} \tag{I.2}$$

The Lagrangian of a free massive Dirac field, namely the electron, is written as follows:

$$\mathcal{L}_0 \quad = \quad i\bar{\Psi}_{\rm e}\gamma^\mu\partial_\mu\Psi_{\rm e} - m_{\rm e}\bar{\Psi}_{\rm e}\Psi_{\rm e} \tag{I.3}$$

where γ^μ are the 4×4 Dirac Gamma matrices satisfying the anti-commutation relation,

$$\{\gamma^\mu, \gamma^\nu\} = 2g^{\mu\nu}\,\mathbf{1}\,, \tag{I.4}$$

and $\bar{\Psi}_{\rm e} \equiv \gamma^0\Psi^\dagger$ is the anti-Dirac spinor, i.e. pozitron, and $\mathbf{1}$ denotes the 4×4 unit matrix in the spinor space. Therefore, the Dirac field $\Psi_{\rm e}(x)$ is a 4-component complex column living in the spin space which means that it has "left" and "right" spin components coupled to each other respectively for electron and its anti-particle pozitron. Thus, a projection operator could be defined in order to seperate the left and right components of the spinor as follows:

$$P_L \equiv \mathbf{1} - \gamma^5\,, \qquad P_R \equiv \mathbf{1} + \gamma^5$$

where $\gamma^5 \equiv i\gamma^0\gamma^1\gamma^2\gamma^3$. Therefore, the left and right components would be defined as follows, respectively:

$${\rm e}_L \equiv P_L\Psi_{\rm e}\,, \qquad {\rm e}_R \equiv P_R\Psi_{\rm e}\,. \tag{I.5}$$

The left electron has the direction of its spin vector and the momentum vector the same while the right electron corresponds to an opposite case. The mass term of the Dirac Lagrangian would be as the following, after the decomposition to left and right components:

$$\mathcal{L}_m \quad = \quad m_{\rm e}\,(\bar{\rm e}_L{\rm e}_R + \bar{\rm e}_R{\rm e}_L) \tag{I.6}$$

Please note that a mass term for a fermion explicitly breaks the global left-right symmetry. The Lagrangian for the free photon field, the so-called Maxwell term, is written as follows:

$$\mathcal{L}_0^{\mathrm{M}} = -\frac{1}{4}F^{\mu\nu}F_{\mu\nu} \tag{I.7}$$

where $F_{\mu\nu} = \partial_\mu A_\nu - \partial_\nu A_\mu$ is the field strength tensor of the electromagnetic field A_μ. The total Lagrangian of the Quantum Electrodynamics would be as the following:

$$\mathcal{L}_{\mathrm{QED}} = \mathcal{L}_0^{\mathrm{D}} + \mathcal{L}_0^{\mathrm{M}} + \mathcal{L}_{\mathrm{int}} \tag{I.8}$$

where the last part is the interaction terms of electron and photon defined as follows

$$\mathcal{L}_{\mathrm{int}} = -iq\bar{\Psi}_{\mathrm{e}}\Psi_{\mathrm{e}}\gamma^\mu A_\mu\,. \tag{I.9}$$

Here, q is the interaction coupling constant to be determined by the experiments. This is the only possible interaction of a Driac field and a photon since higher order terms would make the theory non-renormalizable, i.e., some integral over momenta of a closed loop in the inetraction woul become divergent in perturbative calculations [18].

Now, one may consider a phase transformation by a arbitrary parameter $\theta(x)$ as a function of space-time, as follows:

$$\mathrm{e}_{L,R} \mapsto e^{iq\theta(x)}\mathrm{e}_{L,R}\,, \qquad \bar{\mathrm{e}}_{L,R} \mapsto e^{-iq\theta(x)}\bar{\mathrm{e}}_{L,R} \tag{I.10}$$

where q is a real number corresponding to the physical electric charge of the fermion, extensively written as $q = eQ$ with e the electrical constant and $Q = -1$ for electron. The variance of the free Dirac Lagrangian after this phase transformation would be of the following:

$$\delta\mathcal{L}_0^{\mathrm{D}} = iq\bar{\Psi}_{\mathrm{e}}\Psi_{\mathrm{e}}\gamma^\mu\partial_\mu\theta(x) \tag{I.11}$$

If one imposes that the total Lagrangian, $\mathcal{L}_{\mathrm{QED}}$, should be invariant under the phase transformations, then this implies that the following quantities transform as well:

$$A_\mu \mapsto A_\mu - \partial_\mu\theta(x)\,, \tag{I.12}$$

However, this violates the covariance of the Lagrangian in Eq. (I.8). Therefore, one may redefine a covariant derivative in the Dirac term, as follows:

$$D_\mu \equiv \partial_\mu - iqA_\mu \tag{I.13}$$

This leads the total Lagrangian to be written expicitly as follows:

$$\mathcal{L}_{QED} = i\bar{\mathrm{e}}_L\gamma^\mu D_\mu \mathrm{e}_L + m_\mathrm{e}\bar{\mathrm{e}}_L\mathrm{e}_R + \mathrm{h.c.} - \frac{1}{4}F^{\mu\nu}F_{\mu\nu} \tag{I.14}$$

which is now covariant under an arbitrary phase transformation Eq. (I.10) and Eq. (I.12). This Lagrangian could be extended to any charged fermion like muons, taus, protons, neutrons, etc. instead of only electrons.

I.1.2 Electroweak Inteactions and the Higgs Mechanism

The electromagnetic interaction which describes the dynamics between light and matter, and the weak nuclear interaction which governs the stability of the nucleus are found to be actually originating from a unified interaction in the early universe. This is called Glashow-Weinberg-Salam theory [3–6] of electroweak interactions which includes a mechanism [9–12] that gives masses to the particles, especially to the gauge bosons, via a spinless boson field called the Higgs boson and breaks the symmetry down to QED together with some additional massive bosons responsible for the nuclear forces.

As described in the previous section, QED was an Abelian gauge theory meaning that the gauge boson, i.e. photon, could not interact by itself. On the other hand, the force-carrying bosons of the weak nuclear interaction have a self-inteaction feature, so the gauge group should be non-Abelian.

Considering that the Standard Model includes an SU(2) and an SU(3) gauge groups, first of all it is better to generalize QED discussed in the previous section to a non-Abelian case SU(N). So, one introduces boson fields, W_i, where i runs from 1 to the number of generators N^2-1, and the fermions Ψ, which has N components in the group space.

$$\mathcal{L}^\mathrm{D} = i\bar{\Psi}\not{D}\Psi \tag{I.15}$$

where $\not{D} \equiv \gamma^\mu D_\mu$ and

$$D_\mu = \partial_\mu + igT_iW_{i\mu} \tag{I.16}$$

is the covariant derivative associated with the generators, T_i. Here T_i are the traceless unitary generators, which corresponds to the physical charge, of the non-Abelian group with i running from 1 to N^2-1, so that the following gauge transformations leaves the Lagrangian covariant:

$$\Psi \mapsto e^{igT_i\theta_i(x)}\Psi \tag{I.17}$$

$$W_{i\mu} \mapsto W_{i\mu} + \partial_\mu\theta_i(x) \tag{I.18}$$

for a transformation parameter $\theta_i(x)$ as an extension of Eq. (I.10) and Eq. (I.12).

On the other hand, the kinetic term of the bosons is as follows:

$$\mathcal{L}_W = -\frac{1}{4}W_{i\mu\nu}W_i^{\mu\nu} \tag{I.19}$$

where

$$W_{i\mu\nu} = \partial_\mu W_{i\nu} - \partial_\nu W_{i\mu} + gf_{ijk}W_\mu^j W_\nu^k \tag{I.20}$$

and f_{ijk} are the structure constants that satisfies the commutation relation of the generators of SU(N), namely, $[T_i, T_j] = f_{ijk}T_k$. Note that the self-interaction terms with three and four bosons are embedded in this Lagrangian.

In the case of Glashow-Weinberg-Salam theory, the gauge group would be $\mathrm{U}(1)\otimes\mathrm{SU}(2)$. So, there would be two types of gauge bosons, namely, B^μ from U(1) with a single generator called the hypercharge Y and three W_i^μ from SU(2) with three generators called the isospin T_i for $i = 1, 2, 3$.

The masses of the gauge bosons are explained with the Higgs mechanism which describes a spontaneous symmetry breaking because of a spinless self-interacting boson with a non-zero expectation value in the vacuum. Therefore, the so-called Higgs doublet, is defined as follows:

$$H(x) = \begin{pmatrix} \phi^+(x) \\ \phi^0(x) \end{pmatrix} \tag{I.21}$$

where the neutral component is decomposed into $\phi^0(x) \equiv \nu + h(x)$ and

$$\langle 0|\phi^0|0\rangle \quad = \quad \nu \tag{I.22}$$

is the vacuum expectation value of the Higgs field, with a value of $\nu \approx 246$ GeV. The reason that the Higgs is a SU(2) doublet is because the Higgs would break the symmetry of SU(2) gauge bosons of which it interacts. So, the non-zero expectation value is stemming from the nature of self-interaction of this field, given in the following Lagrangian:

$$\mathcal{L}_H^{\text{int}} \quad = \quad \lambda\left(H^\dagger H - \frac{1}{2}\nu^2\right)^2 \tag{I.23}$$

where, when expanded explicitly, the term $-\frac{1}{4}\lambda\nu^4$ would contribute to the equations of motion as a constant, while the other terms would consist of a negative squared mass term, $-\lambda\nu^2|H|^2$, and a self-interaction four-vertex, $\lambda|H|^4$, for $\lambda > 0$.

The Yukawa interactions, which describes the interaction between a spinless particle and two fermions, reads as follows for the Higgs doublet:

$$\mathcal{L}^Y \quad = \quad -y^{ij}\bar{\Psi}_i H\psi_j + h.c. \tag{I.24}$$

where y^{ij} is the Yukawa coupling of the fermions, Ψ_i and ψ_j which denote a doublet and a singlet of SU(2), respectively. The Yukawa coupling could be written in terms of the fermion's mass as $\frac{m_\psi}{\nu}$ so that it would remain a mass term of the fermion for the vacuum expectation value of the Higgs boson, Eq. (I.22).

Therefore, the full Lagrangian of the Glashow-Weinberg-Salam Model before the symmetry breaking reads as follows:

$$\begin{aligned}\mathcal{L}_{EW}^{\text{symmetric}} \quad = \quad & i\bar{Q}_{iL}\not{D}Q_{iL} + i\bar{u}_{iR}\not{D}u_{iR} + i\bar{d}_{iR}\not{D}d_{iR} + i\bar{L}_{iL}\not{D}L_{iL} + i\bar{e}_{iR}\not{D}e_{iR} \\ & -y_u^{ij}\bar{Q}_{iL}\epsilon H^* u_{jR} - y_d^{ij}\bar{Q}_{iL}Hd_{jR} - y_e^{ij}\bar{L}_{iL}He_{jR} + h.c. \\ & -\frac{1}{4}W_i^{\mu\nu}W_{\mu\nu}^i - \frac{1}{4}B^{\mu\nu}B_{\mu\nu} + \frac{1}{2}\left(D^\mu H\right)^\dagger D_\mu H - \lambda\left(|H|^2 - \nu^2/2\right)^2\end{aligned} \tag{I.25}$$

where ϵ is a 2×2 anti-symmetric matrix assuring the correct component of the Higgs doublet is contributing, and $D_\mu = \partial_\mu - gT_iW_\mu^i - \frac{1}{2}g'YB_\mu$ is the covariant derivative.

The generators of $\text{SU}(2)_L$ are traceless and unitary but only T^3 is diagonal. Therefore,

the W interaction terms of the kinetic term of the Higgs boson would be diagonalized via changing the fields as follows:

$$W^{\pm} \equiv \frac{1}{\sqrt{2}}(W_1 \mp iW_2) \tag{I.26}$$

while the generators would become $T^{\pm} \equiv \frac{1}{\sqrt{2}}\left(T^1 \pm iT^2\right)$. The new fields $W^{\pm}$ are called W bosons and they have opposite weak isospin, i.e. $T^3 = \pm 1$ respectively. The corresponding charged currents are the following:

$$J^{\pm}_{\mu} = \overline{Q}_{iL}\gamma^{\mu}V^{ij}Q_{jL} + \overline{e}_{iL}\gamma^{\mu}e_{iL} \tag{I.27}$$

$$= \overline{u}_i\gamma^{\mu}P_L V^{ij}d_j + \overline{\nu}_i\gamma^{\mu}P_L e_i \tag{I.28}$$

where V_{ij} is the Cabibbo-Kobayashi-Maskawa (CKM) quark mixing matrix [19, 20]. So, the Lagrangian term embedded in the kinetic energy of the fermions would be as $-\frac{g}{\sqrt{2}}J^{\pm}_{\mu}W^{\mu}_{\pm}$.

Here, the quark mixing is an important aspect for the CP violation observed in nature (e.g. Kaon decays). The CKM mixing is a global U(3) phase rotation in the flavour basis of the quarks interacting with the W boson. This phase transformation leaves the mass of the quarks real-valued and positive while reveals a mixture in the W coupling. So, the CKM matrix is written as follows:

$$V_{CKM} = \begin{bmatrix} V_{ud} & V_{us} & V_{ub} \\ V_{cd} & V_{cs} & V_{cb} \\ V_{td} & V_{ts} & V_{tb} \end{bmatrix} \tag{I.29}$$

The parametrization of the matrix has a unremovable complex phase factor which is the only source of the CP violation in the Standard Model.

On the other hand, the remaining W_3 and B bosons would mix by an angle of θ_w, called the weak angle, as follows:

$$Z \equiv \cos\theta_w W_3 - \sin\theta_w B \tag{I.30}$$

$$A \equiv \sin\theta_w W_3 + \cos\theta_w B \tag{I.31}$$

where $e \equiv g\cos\theta_w = g'\sin\theta_w$ is the new coupling constant after the mixing, called the electric coupling constant since it would appear in the following neutral current

interaction:

$$\mathcal{L}_{int}^{NC} = eJ_\mu^{em}A^\mu + \frac{g}{\cos\theta_w}\left(J_\mu^3 - \sin^2\theta_w J_\mu^{em}\right)Z^\mu \tag{I.32}$$

where the electromagnetic current and the neutral weak current is defined as

$$J_\mu^{em} \equiv \sum_\psi q_\psi \bar{\psi}\gamma_\mu\psi \tag{I.33}$$

$$J_\mu^3 \equiv \sum_\psi T_\psi^3 \bar{\psi}\gamma_\mu\psi \tag{I.34}$$

denoting the weak isospin and the electric charge of the fermion ψ by T_ψ^3 and $q_\psi \equiv T^3 + \frac{1}{2}Y$, respectively, as a result of the redefinitions, Eq. (I.30) and Eq. (I.33). See Table I.1 for the values of these charges.

After the symmetry breaking via the Higgs mechanism, the Lagrangian in Eq. (I.25) becomes as follows:

$$\begin{aligned}
\mathcal{L}_{EW}^{\text{broken}} = {} & i\bar{Q}_{iL}\not{D}Q_{iL} + i\bar{u}_{iR}\not{D}u_{iR} + i\bar{d}_{iR}\not{D}d_{iR} + i\bar{L}_{iL}\not{D}L_{iL} + i\bar{e}_{iR}\not{D}e_{iR} \\
& - y_u^{ij}\bar{u}_{iL}hu_{jR} - y_d^{ij}\bar{d}_{iL}hd_{jR} - y_e^{ij}\bar{e}_{iL}he_{jR} + h.c. \\
& - m_u^i\bar{u}_{iL}u_{iR} - m_d^i\bar{d}_{iL}d_{iR} - m_e^i\bar{e}_{iL}e_{iR} + h.c. \\
& - \frac{1}{2}W_i^{+\mu\nu}W_{\mu\nu}^- - \frac{1}{4}A^{\mu\nu}A_{\mu\nu} - \frac{1}{4}Z^{\mu\nu}Z_{\mu\nu} \\
& + \frac{1}{2}\partial^\mu h\partial_\mu h + m_H^2h^2 - \tfrac{gm_H^2}{4m_W}h^3 - \tfrac{g^2m_H^2}{32m_W^2}h^4 \\
& + \left(gm_Wh + \frac{g^2}{4}h^2\right)\left(W_\mu^-W^{+\mu} + \tfrac{1}{2\cos^2\theta_w}Z_\mu Z^\mu\right) \\
& - ig\Big[(W_{\mu\nu}^+W^{-\mu} - W^{+\mu}W_{\mu\nu}^-)(A^\nu\sin\theta_w - Z^\nu\cos\theta_w) \\
& \quad + W_\nu^-W_\mu^+(A^{\mu\nu}\sin\theta_w - Z^{\mu\nu}\cos\theta_w)\Big] \\
& - \frac{g^2}{4}\Big\{\Big[2W_\mu^+W^{-\mu} + (A_\mu\sin\theta_W - Z_\mu\cos\theta_W)^2\Big]^2 - \Big[W_\mu^+W_\nu^- + W_\nu^+W_\mu^- \\
& \quad + (A_\mu\sin\theta_W - Z_\mu\cos\theta_W)(A_\nu\sin\theta_W - Z_\nu\cos\theta_W)\Big]^2\Big\}
\end{aligned} \tag{I.35}$$

where the first line is the kinetic terms with gauge couplings, the second line is the Higgs-fermion couplings, the third line is fermion mass terms, the fourth line is the gauge kinetic terms, the fifth line is the Higgs kinetic energy, mass and self-couplings, the sixth line is the boson-Higgs couplings, the rest of the lines are gauge-gauge couplings.

I.1.3 Strong Interactions

Quantum Chromodynamics (QCD) is the field theory of the strong interactions in an elementary level, i.e. the interaction between quarks (Q_{iL}, u_{iR}, d_{iR}), and gluons (G^a_μ). Since it is a SU(3) gauge theory, the Lagrangian for QCD-only inetractions could be expressed as follows:

$$\mathcal{L}_{\text{QCD}} = g_s\bar{Q}_{iL}\lambda_a G^a_\mu Q_{iL} + g_s\bar{u}_{iR}\lambda_a G^a_\mu u_{iR} + g_s\bar{d}_{iR}\lambda_a G^a_\mu d_{iR} - \frac{1}{4}G^{\mu\nu}_a G^a_{\mu\nu} \quad \text{(I.36)}$$

where only the contribution to the covariant derivative for gluon interaction (i.e., $-ig_s\lambda_a G^a_\mu$, see Eq. (I.16)) is written, and the field strength tensor of the gluons, $G^a_{\mu\nu}$, is in the same form with Eq. (I.20) with the corresponding generators, λ_a, and the strong coupling constant, g_s.

The gluons have 8 different colors. These are generated by the 3×3 matrices, called Gell-mann matrices, λ_a as a color and an anti-color combined in each gluon. In a group theoretical expression,

$$\mathbf{3} \otimes \bar{\mathbf{3}} = \mathbf{8} \oplus \mathbf{1} \quad \text{(I.37)}$$

where $\mathbf{3}$ and $\bar{\mathbf{3}}$ stand for color and anti-color triplet, $\mathbf{1}$ means a color singlet and $\mathbf{8}$ means color octet. The color singlet state, sometimes called the ninth gluon, is not present in the group SU(3), and therefore in the Standard Model, since it is a unit matrix and physically insignificant.

Each (anti)quark is component of a (anti)color triplet labeled as "red", "green" or "blue" as in the following example:

$$u^{\text{red}}_{iL} = \begin{pmatrix} \psi_{iL} \\ 0 \\ 0 \end{pmatrix} \qquad u^{\text{green}}_{iL} = \begin{pmatrix} 0 \\ \psi_{iL} \\ 0 \end{pmatrix} \qquad u^{\text{blue}}_{iL} = \begin{pmatrix} 0 \\ 0 \\ \psi_{iL} \end{pmatrix} \quad \text{(I.38)}$$

On the other hand, gluons are spanned by 3×3 Gell-mann matrices, so that the quarks having the appropriate color charges would interact with that gluon. So, each component

of the octet, $\mathbf{G}_\mu \equiv \lambda_a G^a_\mu$, reads explicitly as follows:

$$
\begin{aligned}
\mathbf{G}^{\mathrm{rg}}_\mu &= \begin{bmatrix} 0 & G^1_\mu & 0 \\ G^1_\mu & 0 & 0 \\ 0 & 0 & 0 \end{bmatrix} & \mathbf{G}^{\mathrm{gr}}_\mu &= \begin{bmatrix} 0 & -iG^2_\mu & 0 \\ iG^2_\mu & 0 & 0 \\ 0 & 0 & 0 \end{bmatrix} \\
\mathbf{G}^{\mathrm{rr}}_\mu &= \begin{bmatrix} G^3_\mu & 0 & 0 \\ 0 & -G^3_\mu & 0 \\ 0 & 0 & 0 \end{bmatrix} & \mathbf{G}^{\mathrm{rb}}_\mu &= \begin{bmatrix} 0 & 0 & G^4_\mu \\ 0 & 0 & 0 \\ G^4_\mu & 0 & 0 \end{bmatrix} \\
\mathbf{G}^{\mathrm{br}}_\mu &= \begin{bmatrix} 0 & 0 & -iG^5_\mu \\ 0 & 0 & 0 \\ iG^5_\mu & 0 & 0 \end{bmatrix} & \mathbf{G}^{\mathrm{bg}}_\mu &= \begin{bmatrix} 0 & 0 & 0 \\ 0 & 0 & G^6_\mu \\ 0 & G^6_\mu & 0 \end{bmatrix} \\
\mathbf{G}^{\mathrm{gb}}_\mu &= \begin{bmatrix} 0 & 0 & 0 \\ 0 & 0 & -iG^7_\mu \\ 0 & iG^7_\mu & 0 \end{bmatrix} & \mathbf{G}^{\mathrm{rgb}}_\mu &= \begin{bmatrix} \frac{1}{\sqrt{3}}G^8_\mu & 0 & 0 \\ 0 & \frac{1}{\sqrt{3}}G^8_\mu & 0 \\ 0 & 0 & -\frac{2}{\sqrt{3}}G^8_\mu \end{bmatrix}
\end{aligned}
\tag{I.39}
$$

Note that the QCD Lagrangian, Eq. (I.36), and the EW Lagrangian, Eq. (I.25) or Eq. (I.35), are indeed discrete since in each definition the covariant derivatives were given accordingly, so that the SM Lagrangian could be written as a sum of the two, as follows:

$$
\mathcal{L}_{\mathrm{SM}} = \mathcal{L}_{\mathrm{QCD}} + \mathcal{L}_{\mathrm{EW}} \tag{I.40}
$$

I.2 Top Quark

The top quark, together with the bottom quark, theoretically predicted in 1973 by T. Maskawa and M. Kobayashi to explain the Charge-Parity (CP) violation in Kaon decay, extending the Cabbibo quark-mixing matrix to a three-generation quark-mixing matrix, now called the Cabbibo-Kobayashi-Maskawa (CKM) matrix. Then, the top quark discovered in 1995 by the DØ and CDF experiments at FermiLab.

The top quark is the heaviest particle that is known so far, and as well as among other Standard Model particles, with a mass of 173 GeV. The electrical charge is $Q_t = +2/3$, having an hypercharge of $Y = 4/3$ (or $1/3$) and a weak isospin of $T^3 = 0$ (or $1/2$) for the right (or left) component. The Higgs coupling of top quark is around 0.7 which is the largest among other fermions.

The top quark has a special place in the Standard Model of particle physics and plays a promising role to extend the current boundaries to the new physics. The following considerations of the top quark reveals the search for new physics:

- The top quark is the heaviest particle, which also means that it has the strongest Yukawa coupling among the fermions of the Standard Model. This is promising for seeking new strong dynamics since it is directly related to the breaking of the electroweak symmetry.
- The loop corrections to the Higgs boson mass includes a top quark loop which opens a window to the tera-scale physics, e.g. SUSY, Little Higgs models.
- The rapid decay of the top quark gives a unique route to investigate the nature of a "bare quark" related to its mass, charge and spin.
- The decays of top quark to the heavy states like W, Z or Higgs boson plus a quark have a very large phase space due the high top mass.
- The coupling of the top quark with the W boson offers an opportunity to explore the models beyond the three-generation quarks by directly measuring the CKM mixing matrix element.

The top-quark part of the Standard Model Lagrangian, Eq. (I.40), reads explicitly as follows:

$$
\begin{aligned}
\mathcal{L}_{\mathrm{SM,top}} &= i\bar{t}\gamma^{\mu}\partial_{\mu}t && \text{Propagation} \\
&- m_t\bar{t}t && \text{mass term} \\
&- \tfrac{m_t}{v}\bar{t}Ht && \text{Higgs coupling} \\
&+ g_s\bar{t}\gamma^{\mu}\lambda^a G^a_{\mu}t && \text{gluon coupling} \\
&+ e\bar{t}\gamma^{\mu}QA_{\mu}t && \text{photon coupling} \\
&+ \tfrac{g}{\cos\theta_w}\bar{t}\gamma^{\mu}\left(g_V + g_A\gamma^5\right)Z_{\mu}t && \text{Z-boson coupling} \\
&+ \tfrac{g}{\sqrt{2}}\sum_{q}^{d,s,b} V_{tq}\bar{t}\gamma^{\mu}P_L W^-_{\mu}q + \text{h.c.} && \text{CKM-mixed W-boson coupling}
\end{aligned}
\tag{I.41}
$$

where $g_V = \frac{1}{2}T^3 - Q\sin^2\theta_w$ and $g_A = -\frac{1}{2}T^3$ are the vectoral and axial couplings to Z boson, respectively.

Considering the radiative one-loop corrections to the W boson mass, the top mass contributes significantly together with the Higgs boson mass:

$$m_W^2 = \frac{\pi\alpha}{\sqrt{2}G_F \sin^2\theta_w (1-\Delta r)} \tag{I.42}$$

where G_F is the Fermi constant and the correction is calculated as follows:

$$\Delta r = -\frac{3G_F m_t^2}{8\sqrt{2}\pi^2 \tan^2\theta_w} + \frac{3G_F M_W^2}{8\sqrt{2}\pi^2}\left(\ln\frac{M_H^2}{M_Z^2} - \frac{5}{6}\right) \tag{I.43}$$

Therefore, one could reveal a relation between the top mass and the Higgs mass for the given W and Z masses.

I.2.1 Decays

In the Standard Model, top quark decays only via weak interaction to a W boson and a down-type quark, dominantly a b quark. The full decay rate for the top quark is calculated as follows:

$$\Gamma\left(t \to W^+ q\right) = \frac{|V_{tq}|^2 m_t^3}{16\pi\nu^2}\left(1+2\frac{M_W^2}{m_t^2}\right)\left(1-\frac{M_W^2}{m_t^2}\right)^2\left(1-\frac{\alpha_s(4\pi^2-15)}{9\pi}\right) \tag{I.44}$$

where α_s is the fine structure constant of the strong interactions. The branching ratio for the Wb decay is directly related to the CKM mixing parameter as follows:

$$\frac{B(t\to Wb)}{B(t\to Wq)} = \frac{|V_{tb}|^2}{|V_{tb}|^2+|V_{ts}|^2+|V_{td}|^2} \tag{I.45}$$

which is measured to be 0.91 ± 0.04, means that approximately the 90% of the top quarks decays into a b quark. Since the Standart Model predicts 3 generation of quarks, the constraint $|V_{tb}|^2+|V_{ts}|^2+|V_{td}|^2=1$ might be considered for precise measurements of the CKM matrix element $|V_{tb}|$. On the other hand, without the assumption of three-generation quarks, the ratio opens a window for extra-generation quarks directly.

An important aspect of the decay rate given above is that the top quark decays so promptly even before hadronization because the value of the decay rate is greater than the QCD threshold:

$$\Gamma\left(t \to W^+ q\right) = 2.0^{+0.7}_{-0.6}\,\text{GeV} > \Lambda_{\text{QCD}} \tag{I.46}$$

where $\Lambda_{\mathrm{QCD}} \approx 250$ MeV. This also implies that the lifetime of the top quark is $0.5 \times 10^{-24}s$ which is long before the colorless boundstates can form or even before moving away from the interaction vertex into the detector. So, the top quark, as the only known particle to decay before hadronization, gives the unique opportunity to understand the properties of a "bare quark".

The top quark events are categorized according to the decay modes of the W boson stemming from the top quark because the W boson has a short lifetime, approximately $3 \times 10^{-25}s$, and this means it can not be directly measured in the detectors. Instead the decay products of the W boson should be studied to understand the top quark events.

W boson decays mostly into two quarks which are hadronized to produce jets which is a shower of variety of hadrons might be stopped in the calorimeters of the detector. This decay mode is called "hadronic top decay" and it is hard to separate since there would be a large number of background events with very similar jet topologies. Another decay mode is "leptonic top decay" which means the W boson produces a charged lepton and its associated neutrino. It is called "electron (muon) channel" when the lepton in subject is electron (muon).

I.2.2 Top Quark Production

There are two ways to produce top quark in proton-proton collisions, one via charged-current electroweak interactions as a single, and another via strong interactions as a pair. For this reason, the single top-quark production allows to probe the electroweak sector of the Standard Model with top-quark physics.

Pair production

The top-pair production is either a quark-antiquark anhillation, $q\bar{q} \rightarrow \mathrm{t\bar{t}}$, or a gluon fusion, $gg \rightarrow \mathrm{t\bar{t}}$. An event where the both W bosons decay into quarks is called "fully hadronic" while one or two of the W bosons decay into leptons are called "semi-leptonic" or "di-leptonic", respectively.

Since hadronic collisions have the hard process via the interaction of the constitutent quarks and gluons which are called partons, the total cross-section of the pair production at a center of mass energy $\sqrt{s}$ could be expressed as a convolution of two contributions.

One contribution is the short-distance interaction between the participating partons at the center of mass energy $\sqrt{\hat{s}}$, while the other contribution comes from the long-distance factors that specify the probability density of observing these partons with a certain fraction in the momenta of the incoming hadrons, as follows:

$$\sigma_{pp\to t\bar{t}} = \sum_{i,j}^{q,\bar{q},g} \int dx_i dx_j \underbrace{f_i\left(x_i,\mu_F^2\right)\overline{f}_j\left(x_j,\mu_F^2\right)}_{\text{long-distance}} \underbrace{\sigma_{ij\to t\bar{t}}\left(x_i,x_j\right)}_{\text{short-distance}} \tag{I.47}$$

where x_i is the hadron longitudinal momentum fraction carried by the parton i running for all quarks, anti-quarks and gluons, μ_F^2 is the factorization scale, $f_i(x_i,\mu^2)$ are the Parton Distribution Functions (PDFs) of the proton, which is simply the probability density to observe a parton i with the momenta fraction x_i such that $\hat{s} = x_i x_j s$, and $\sigma_{ij\to t\bar{t}}$ is the cross-section of the hard process of the partons producing the top pair.

The hard process, which involves only high momentum transfer and almost insensitive to low momentum scale, is calculable with perturbative QCD. The factorization is valid to all orders of the perturbative theory, getting weaker dependence on the arbitrary scale μ_F^2 as more perturbative terms are added in the expansion. On the other hand, the PDFs characterizing the long-distance process can not be calculated in perturbative QCD, instead are extracted by global fits from deep-inelastic scattering and other data.

The minimum $\hat{s} = x_i x_j s$ in the process is $4m_t^2$ and therefore $x_i x_j \geq 4m_t^2/s$ which will typically be near the threshold for the $t\bar{t}$ production since the probability of finding a parton with fraction x decrease with increasing x. This means that $\langle x\rangle \approx \sqrt{x_i x_j} \approx 2m_t/\sqrt{s}$ would be 0.18 at TeVatron and 0.25 at the LHC, and explains why we observe a dominance of the quark-antiquark annhilation with 85% at TeVatron, but on the other hand, the gluon fusion with 90% at LHC.

The cross-sections calculated for 7, 8, 13 and 14 TeV collision energies are presented in Table I.2.

Cross-Section (pb)	7 TeV	8 TeV	13 TeV	14 TeV
$\sigma_{pp\to t\bar{t}}$	174^{+11}_{-12}	248^{+14}_{-15}	810^{+38}_{-36}	957^{+44}_{-41}

TABLE I.2: Table of the Standard Model predictions for the top-pair production cross-sections at NNLO with NNNLL self-gluon corrections [21].

Single Production

Three different mechanisms for single top-quark production are predicted in the SM in hadron-hadron collisions according to the virtuality of the W boson (Figure I.1):

- s-channel production as $q^2 > 0$.
- W-associated, or tW production as $q^2 = m_W^2$.
- t-channel production as $q^2 < 0$.

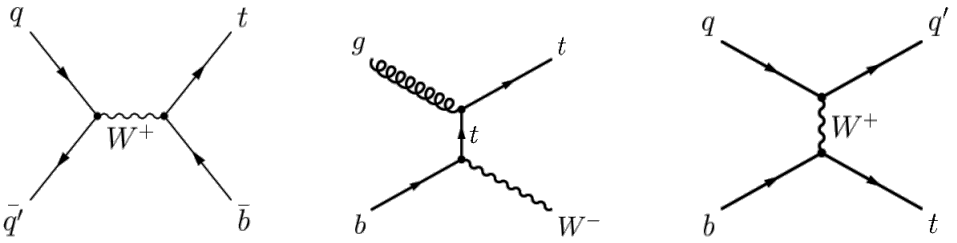

FIGURE I.1: The single top-quark production in s-channel (left), W-associated t-channel (middle) and t-channel (right).

All three channels are directly related to the CKM matrix element $|V_{tb}|$, providing the chance for a direct measurement of this SM quantity. There is a special interest in LHC for s-channel single-top production since it is very sensitive to several models of new physics involving fourth-generation quarks, a non-SM mediator, like W′ or a charged Higgs boson.

Cross-Sections (pb)	7 TeV	8 TeV	13 TeV	14 TeV
t-channel	$65.9^{+2.6}_{-1.8}$	$87.2^{+3.44}_{-2.42}$	$219.1^{+6.7}_{-3.9}$	243^{+8}_{-6}
tW-channel	15.6 ± 1.17	22.2 ± 1.52	$58.5^{+2.4}_{-3.1}$	$83.6^{+3.6}_{-5.2}$
s-channel	$4.56^{+0.19}_{-0.18}$	5.55 ± 0.22	$10.22^{+0.22}_{-0.21}$	$11.92^{+0.49}_{-0.53}$

TABLE I.3: Table of the Standard Model predictions for the single top production cross-sections for all three production channels at NNLO [22–26].

According to the cross-section calculations of the single-top production as shown in Table I.3, the t-channel searches will benefit mostly in the LHC Run II which will have 13 and 14 TeV collision energies.

I.2.3 Experimental Results

All the measurements done so far are in an agreement with the Standard Model predictions listed in Table I.3. The finalized experiments CDF and D0 Collaborations at Tevatron with 1.96 TeV center-of-mass energy and the current experiments ATLAS and CMS Collaborations at CERN with 7 TeV and 8 TeV center-of-mass energies have reported several results given below.

Observation of single top-quark production was published by the CDF [27–29] and D0 [30, 31] collaborations in the sum of the s- and the t-channels. Subsequently, The CDF collaboration reported a measurement of single top-quark production cross-section for the sum of s-, t-, and Wt-channels as $3.04^{+0.57}_{-0.53}$ pb using data corresponding to 7.5 fb^{-1} of integrated luminosity [32] and for the sum of the s- and t- channels as $3.02^{+0.49}_{-0.48}$ pb using up to 9.5 fb^{-1} of integrated luminosity [33]. The D0 collaboration obtained a cross-section of $4.11^{+0.60}_{-0.55}$ pb using data corresponding to 9.7 fb^{-1} of integrated luminosity [34].

The cross sections for each production mode were also measured separately. The D0 collaboration measured the cross-section of the t-channel process to be $3.07^{+0.54}_{-0.49}$ pb using data corresponding to 9.7 fb^{-1} of integrated luminosity [34, 35]. On the other hand, the CDF collaboration measured t- and tW-channels as $1.66^{+0.53}_{-0.47}$ pb using data corresponding to 7.5 fb^{-1} of integrated luminosity [32] and t-channel as $1.65^{+0.38}_{-0.36}$ pb using up to 9.5 fb^{-1} [33] of integrated luminosity. Furthermore, CDF and D0 combined their results [36–38] to observe the s-channel process with $1.29^{+0.26}_{-0.24}$ pb [38].

At the LHC proton-proton collider, t-channel production at 7 TeV center-of-mass energy was observed to be 84^{+20}_{-19} pb by the ATLAS collaboration [39, 40] and 83.6 ± 30.0 pb by the CMS collaboration [41]. The 8 TeV measurements in t-channel was reported as 95 ± 18 pb by ATLAS [42] and $80.1^{+12.3}_{-7.0}$ pb by CMS collaborations [43]. Furthermore, ATLAS has found evidence for Wt-channel production [44], followed recently by an observation at the CMS experiment[45, 46]. The s-channel at $\sqrt{s} = 8$ TeV in ATLAS has been measured to be 5.0 ± 4.3 pb [47] and in the CMS to be $6.2^{+8.0}_{-5.1}$ pb which is also presented in this work [48]. The CKM matrix element $|V_{tb}|$ is extracted as 0.998 ± 0.041 at $\sqrt{s} = 7$ TeV [49].

Chapter II

The Experiment: LHC and CMS

The Lagrangian describes the interactions of a field theory as discussed in Sec. I.1. On the other hand the experiments attempt to measure the rate at which a specified interaction occurs. The bridge between a field theory and experiment is the cross-section for the interaction in subject, which gives the expected number of the events, N, that will result from the collision of a large number of particles.

The cross-section, σ, may be calculated from the Lagrangian using the method of the field theory to produce a prediction that might be tested at a collider experiment such as LHC. The number of events, N, for a specified interaction, namely the "signal", is given by the following:

$$N_{\text{signal}} = \sigma_{\text{signal}} \varepsilon \int dt L \tag{II.1}$$

where ε is the efficiency of the detector, L is the luminosity, which is defined as the number of particles per unit area per second in the colliding beams, and σ_{sig} is the cross-section. Here the luminosity is integrated over time so that it gives the total number of interactions occured. The cross-section is in units of area, namely "barn", which is defined as $1\text{b} = 10^{-28} m^2$, tipically measured in femtobarns (fb) or picobarns (pb) in high energy physics. Therefore the integrated luminosity is in the units of inverse area, tipically given in pb^{-1} or fb^{-1} for LHC experiments.

II.1 The Large Hadron Collider

The Large Hadron Collider (LHC) at the European Centre for Nuclear Research (CERN) is a two-ring superconducting proton-proton collider situated in the 27 km tunnel previously constructed for the Large Electron-Positron collider (LEP) [50, 51]. The first beam operation was launched in 2008 with a design to provide proton-proton collisions with a luminosity of $10^{34}\text{cm}^{-2}\text{s}^{-1}$ and a unprecedented centre-of-mass energy of 14 TeV for the study of rare events, such as the production of the Higgs particle which was observed recently in 2012.

The LHC has two general purpose experiments ATLAS and CMS, aiming to collect data with high luminosity, and two experiments, LHCb for B-physics and TOTEM for the detection of protons from elastic scattering at small angles, working at lower luminosities of $10^{32}\text{cm}^{-2}\text{s}^{-1}$ and $10^{29}\text{cm}^{-2}\text{s}^{-1}$, respectively. In addition to proton-proton operation, the LHC is able to collide heavy nuclei, Pb-Pb, with a total centre-of-mass energy of 1150 TeV which corresponds to 2.76 TeV per nucleon, and for this it has one dedicated ion experiment, ALICE, aiming at a peak luminosity of $10^{27}\text{cm}^{-2}\text{s}^{-1}$.

The LHC is decided to be operated at the reduced beam energy of 3.5 TeV for the first two years after an accident occured in 19 September 2008, just 9 days after the very first beam, which caused substantial damage to the magnets and to the beam pipe imposed an intervention of repairs and improvements. Following the pilot runs at 0.9 and 2.36 TeV collision energies, LHC performed the first collision at 7 TeV on 30 March 2010, initially at a low luminosity of about $1 \times 10^{27}\text{cm}^{-2}\text{s}^{-1}$ to reach immediately to a luminosity of $3.6 \times 10^{33}\text{cm}^{-2}\text{s}^{-1}$ in October 2010. The integrated luminosity was recorded by experiments as 44pb^{-1} in 2010, 6fb^{-1} in 2011, and 23fb^{-1} in 2012, as shown in Figure II.1.

The LHC simultaneously accelerates two proton (or lead) beams circulating in opposite directions, so the magnets use a twin bore design to bend particles in both beams simultaneously. There are eight crossing points around the ring where beams can be crossed together to produce collisions, although only four of these are currently in use by LHC experiments.

Protons are initially produced in a duoplasmatron source where electrons that are emitted from a cathode filament hit gaseous hydrogen atoms. Then the protons pass through a chain of accelerators starting from the injection into the linear accelerator Linac2 to

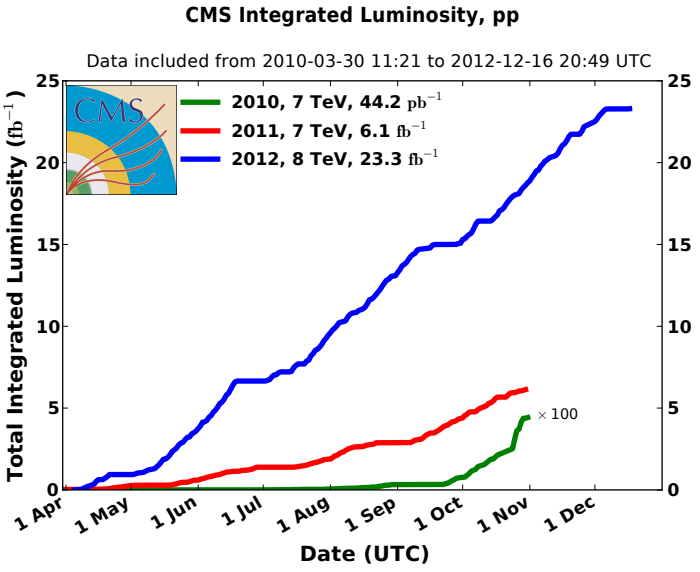

FIGURE II.1: The total integrated luminosity recorded by the CMS experiment in 2010, 2011 and 2012.

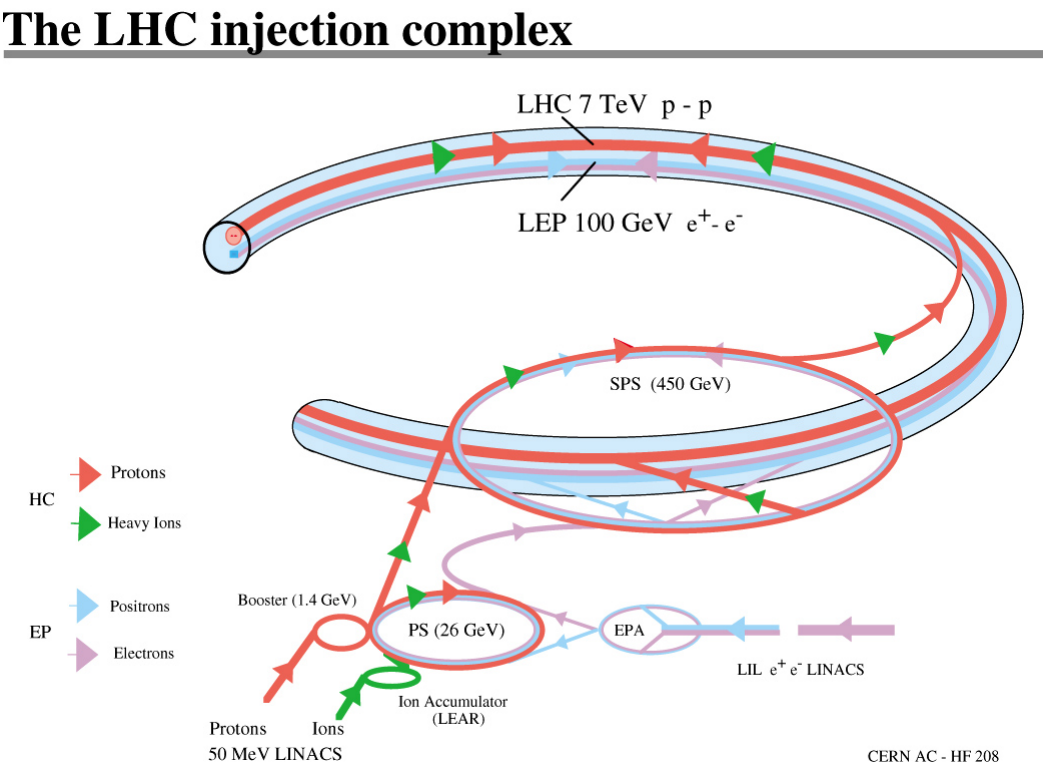

FIGURE II.2: The LHC injection complex.

reach a preliminary energy of 50 MeV. Then the Proton Synchrotron Booster takes the protons to 1.4 GeV and passes them to the Proton Synchrotron where they are accelerated to 25 GeV. Before they enter into the LHC in the final stage, the Super Proton Synchrotron, the protons reach 450 GeV.

On the other side, lead ions are formed in an Electron Cyclotron Resonance and later accelerated in Linac3. After they are accelerated in the Low Energy Ion Ring, they are passed to Proton Synchrotron Booster where the protons accelerated as well. So, the remaining stages follow the same as the proton beam as shown schematically in Figure II.2.

After the two rings are filled, the machine is ramped to its nominal energy of 7 TeV over about 28 min. In order to reach this energy, the dipole field must reach the level for accelerator magnets of 8.3 T. This high field can only be achieved using the superconducting material NbTi, by cooling the magnets in superfluid helium at a tempreture lower than 2K.

II.1.1 Design and Layout

The basic layout of the LHC follows the LEP tunnel geometry and is shown in Figure II.3. The machine has eight arcs and straight sections, the last being approximately 528m long. Four of the straight sections house the LHC detectors while the other four are used for machine utilities, radio frequency and collimation systems, and beam dump insertions. The two high luminosity detectors are located at diametrically opposite straight sections. The ATLAS detector is located at point 1 and CMS at point 5, which also incorporates the small angle scattering experiment TOTEM. Two more detectors are located at point 2 (ALICE) and at point 8 (LHCb), which also contain the injection systems for the two rings. The beams only cross from one ring to the other at these four locations.

The number of events taking place per second at the LHC interaction point is given by

$$N = \sigma L \tag{II.2}$$

where σ is the cross-section of the process in subject and L is the luminosity which is expressed as the following:

$$L = \frac{n_b n_1 n_2 f_{\text{rev}}}{2\pi \Sigma_x \Sigma_y} F \gamma_r$$

where γ_r is the relativistic gamma factor, F is the geometric luminosity reduction factor due to the crossing angle at the interaction point, n_b is the number of bunches per beam, n_1 and n_2 are the number of particles per bunch, f_{rev} is the revolution frequency,

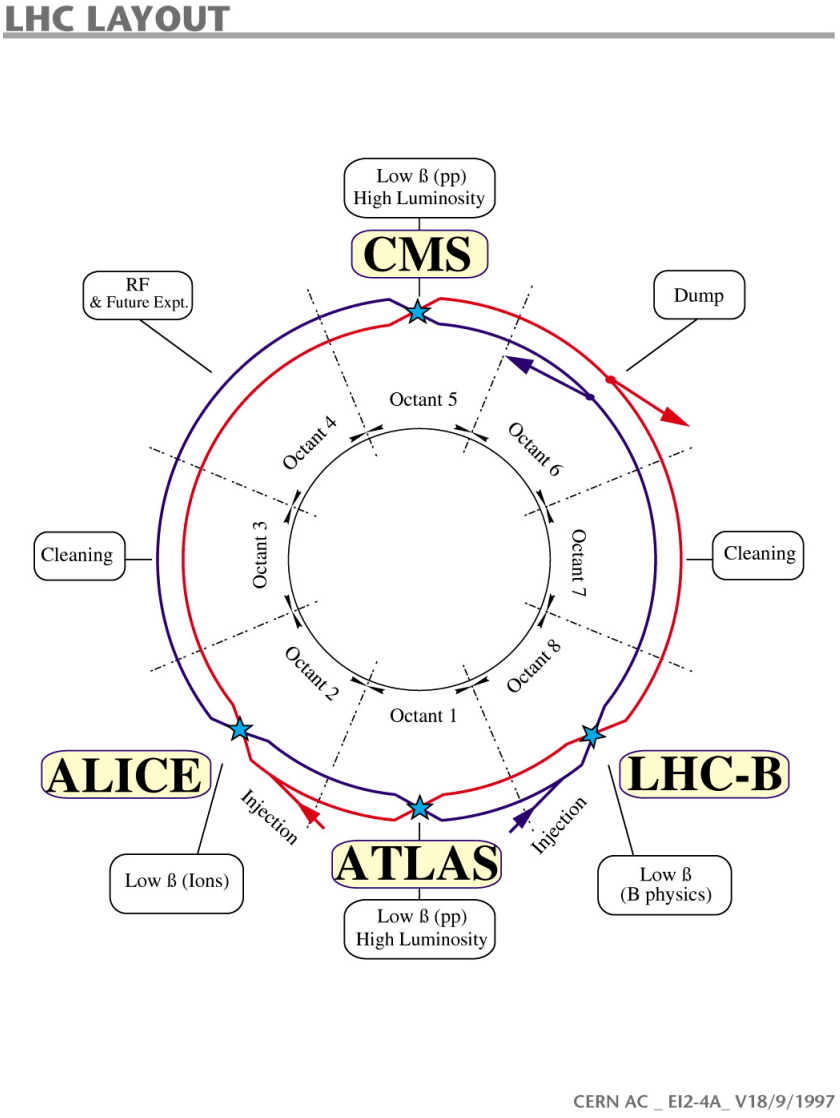

FIGURE II.3: The LHC layout.

and the factors $\Sigma_{x,y}$ represent the horizontal and the vertical convolved beam widths, respectively. When the machine reaches the desinged peak luminosity of $10^{34}\text{cm}^{-2}\text{s}^{-1}$ for the detectors CMS and ATLAS, the number of particles per bunch would reach $n_{1,2} = 1.15\times10^{11}$ while the number of bunches per beam would be 2808 with a revolution frequency of 11245 Hz.

II.1.2 Magnets

The LHC contains more than 7000 superconducting magnets ranging from the 15m long main dipoles to the 10 cm octupole/decapole correctors inside the dipole cold masses as well as more than 100 conventional warm magnets and the about 500 conventional

magnets in the two 2.6 km long transfer lines between the SPS and the LHC . The LHC magnet system, while still making use of the well-proven technology based on NbTi Rutherford cables, cools the magnets to a temperature of 1.8 K, using superfluid helium, and operates at fields above 8 T. This so low temperature with respect, for example, to the other large superconducting accelerators, Tevatron, HERA and RHIC which cools the magnets down to 4.5 K, brings a decrease of the heat capacity of the superconductor by an order of magnitude, making the magnets more sensitive to quenches.

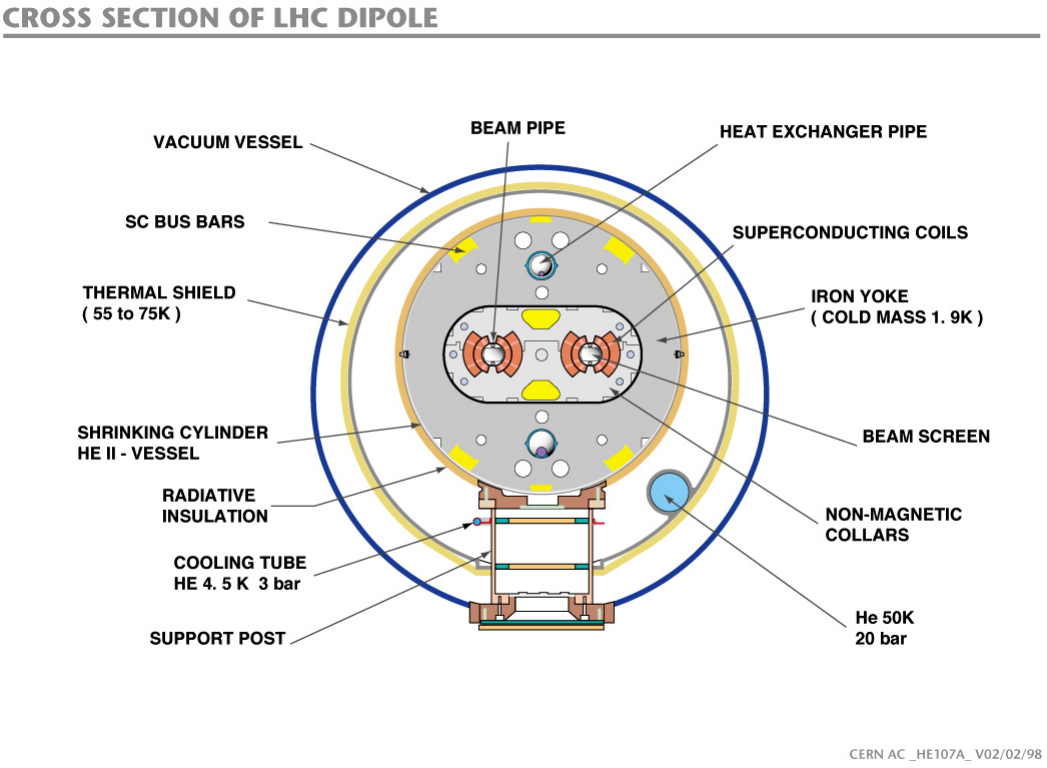

FIGURE II.4: The LHC dipole cross-section [52].

II.1.3 Vacuum System

The design of the beam vacuum system takes into account the requirements of 1.9 K operation and the need to shield the cryogenic system from heat sources, as well as the usual constraints set by chamber impedances. The main heat sources are the synchrotron light radiated by the beam, the image currents, the development of electron clouds and the energy loss by nuclear scattering. Intercepting these heat sources at a temperature above 1.9 K has necessitated the introduction of a beam screen cooled to between 5 and 20 K. This beam screen is perforated in about 4% of the surface area to allow the cold bore of the magnets at 1.9K to act as a distributed cryopump. The slots in the beam

screen are displaced in a pseudorandom pattern to avoid periodic perturbations which can induce resonant beam modes.

II.1.4 RF Acceleration System

The RF system is located at point 4. Two independent sets of cavities operating at 400 MHz (twice the frequency of the SPS injector) allow independent control of the two beams. The superconducting cavities are made from copper whose internal surface is sputtered with a thin film of a few microns of niobium. In order to combat the intrabeam scattering (see below), each RF system must provide 16 MV during coast while at injection 8 MV is needed. Although the RF hardware required is much smaller than LEP due to the very small synchrotron radiation power loss, the real challenges are in controlling beam loading and RF noise.

II.1.5 Accelerator Physics

Here, some effects of the issues in the accelerator physics on the machine is presented briefly.

Coherent instabilities

The interaction of the beam with its environment generates electromagnetic fields which can react back on the beam and drive it unstable. The first step is to design the vacuum chamber to reduce this coupling as much as possible, for instance reducing the resistivity of the copper in the beam screen by cooling it to between 5 and 20 K, or making the chamber smooth without discontinuities.

Nevertheless reducing the resistivity of the environment can reduce but not definitely avoid the growth of the instabilities. The two main instabilities to be kept under control are the transverse coupled bunch instability and the single bunch head-tail instability. Without giving too much detail, the former is due to image currents in the beam screen and its main unstable modes are damped through the action of a pair of electrostatic deflectors. The latter, head-tail effect, is an instability due to the short range wakefields acting between the tail and the head of the bunch. It is taken under control by the action of sextupoles integrated into the short straight sections.

Finally, the Landau damping, which acts on very high frequency oscillation modes, is provided with two families of strong octupoles without need for feedback and, for this reason, it is particularly important when the transverse feedback system has noise problems.

Dynamic aperture

In superconducting magnets of the type used in the LHC, the field quality is determined by the precision of the positioning of the superconductor. It has been shown that the aperture inside which particles orbits are stable, is much smaller than the physical aperture of the beam pipe. It is called dynamic aperture and is limited mainly by the unwanted higher field harmonics due to magnet imperfections. Although sophisticated computer simulations take into account these effects, it is not possible to perform the full scale simulation over 4×10^7 turns, which correspond to 1 h of storage time. So, in order to insure a dynamic aperture of 6 sigmas, it has been decided to use the tracked dynamic aperture evaluated over 10^6 turns multiplied by a factor of 2.

The beam-beam interaction

The maximum particle density per bunch is limited by the nonlinear beam-beam interaction that each particle experiences when the bunches of both beams collide with each other. It reveals a variation of the tune with amplitude, and the excitation of nonlinear resonances due to the periodic nature of the force. The linear tune shift can be expressed by:

$$\zeta = \frac{n_b r_p}{4\pi\epsilon_n} \tag{II.3}$$

where n_b is the number of bunches per beam, ϵ_n is the normalized transverse beam emittance, r_p is the classical proton radius given by $r_p = e^2/4\pi\epsilon_0 m_p c^2$ in which e is the electron charge, ϵ_0 is the electric permeability and m_p is the proton mass. Experience with hadron colliders indicates that the total linear tune shift summed over all interaction points should not exceed 0.015, and in the LHC case, the tune shift must be $\zeta < 0.005$. The long range beam-beam interactions between successive bunches are also reduced by colliding the beams with a small crossing angle of about 400 μrad.

II.2 The Compact Muon Selenoid

The Compact Muon Solenoid (CMS) detector is a multi-purpose apparatus operating at the Large Hadron Collider at CERN [53]. The total proton-proton cross-section at $\sqrt{s} = 14$ TeV is expected to be roughly 100 mb. At design luminosity the general-purpose detectors will therefore observe an event rate of approximately 10^9 inelastic events / s, leading to a number of formidable experimental challenges. The online event selection (trigger) must reduce the huge rate to about 100 events / s for storage and analysis. Furthermore, at design luminosity we expect a mean of about 20 inelastic collisions per bunch crossing and so around 1000 charged particles will emerge from the interaction region every 25 ns (time between two successive bunch crossing). The superimposition of other events on the event of interest, the so called pile-up effect, can be reduced by using high granularity detectors with good time resolution and low occupancy. This would inevitably require the use of millions of detector electronic channels which need very good synchronization.

II.2.1 Detector Design

The detector design and layout 2.7 is mainly driven by the choice of the magnetic field configuration, needing for large bending power to precisely measure high energy particles momentum. The heart of CMS detector is the big 4 T superconducting solenoid which accommodates the inner tracker and calorimetry inside and is situated immediately before the muon detectors.

II.2.2 Superconducting Magnets

The CMS superconducting solenoid 2.10 has been designed to reach a 4 T field in a free bore of 6 m diameter and 12.5 m length with a stored energy of 2.6 GJ at full current. The flux is returned through a 10000-t yoke containing 5 wheels and 2 endcaps. The distinctive feature of the 1.8 K, 220-t cold mass is the 4-layer winding made from a stabilized reinforced NbTi conductor, needed to be able to reach the desired 4 T magnetic field. The ratio between stored energy and cold mass is high as 11.6 KJ/kg, causing a large mechanical deformation of 0.15% during energizing.

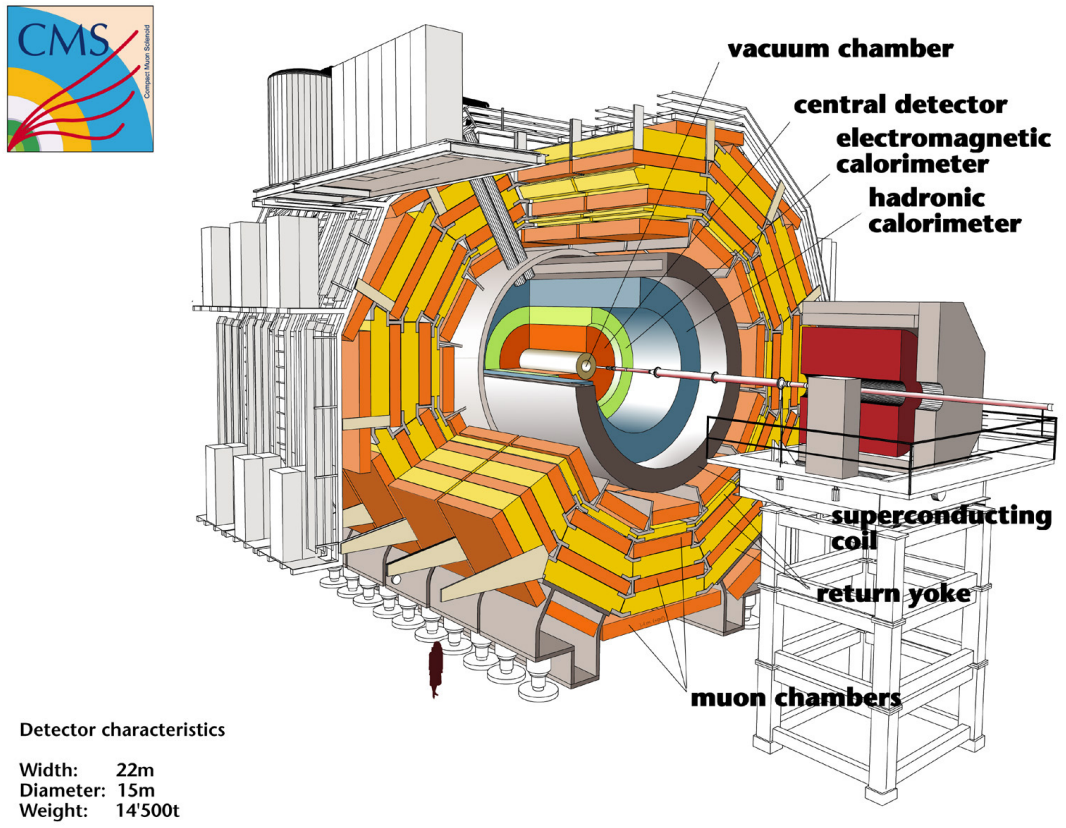

FIGURE II.5: The design of the Compact Muon Selenoid.

II.2.3 Tracking System

The inner tracking system of CMS is designed to provide a precise and efficient measurement of the trajectories of charged particles coming from the LHC collisions, as well as a precise reconstruction of secondary vertices [54]. The tracker which is fully covered by the solenoid magnetic field surrounds the interaction region and has a length of 5.8 m and a diameter of 2.5 m. The high rate of interactions requires high granularity and fast response as well as efficient cooling system and radiation hardness, aspects which led to the silicon technology choice.

The pixel detector in the inner part contains three barrel layers at radii of 4.4, 7.3, and 10.2 cm, respectively, with a length of 53 cm each. The two endcaps for each side are located at $|z| = 34.5$ cm and $|z| = 46.5$ cm and extend in r from 6 to 15 cm. The pixel size is $100 \times 150\,\mu\text{m}^2$. The strip detector is divided into an inner part and outer part, both divided further into the barrel part and discs that cover the forward region which are called Tracker Inner Barrel (TIB), Tracker Inner Disks (TID), Tracker Outer Barrel (TOB), and Tracker Endcaps (TEC), as shown in Figure II.6.

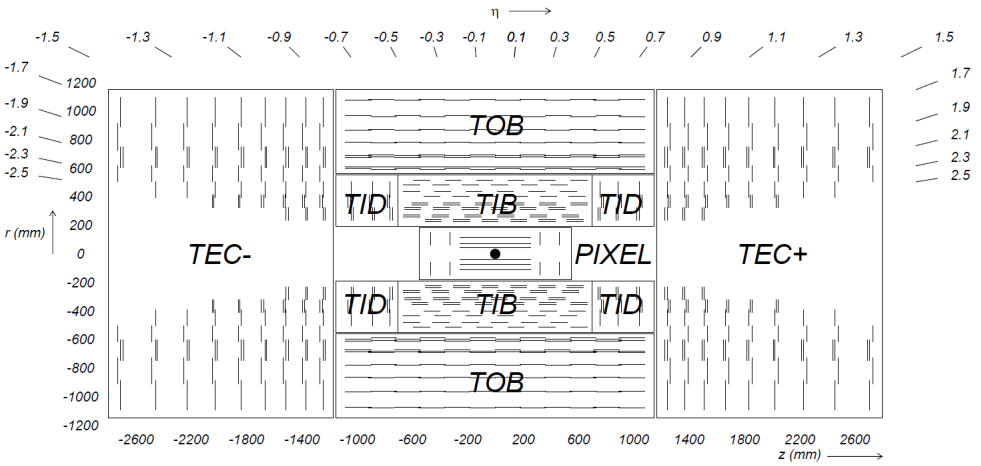

FIGURE II.6: The tracker system.

II.2.4 Electromagnetic Calorimeter

The electromagnetic calorimeter of CMS (ECAL) is a hermetic homogeneous calorimeter made of 61200 lead tungstate crystals, $PbWO_4$, mounted in the central barrel part, 7324 crystals in each of the two endcaps and a preshower detector placed in front of the endcap crystals, mainly for π^0 identification [55]. Avalanche photodiodes (APDs) are used as photodetectors in the barrel and vacuum phototriodes (VPTs) in the endcaps. The high density of crystals give the calorimeter the characteristics of fast response, fine granularity and radiation resistance, as well as a good capability to detect the decay to two photons of the postulated Higgs boson.

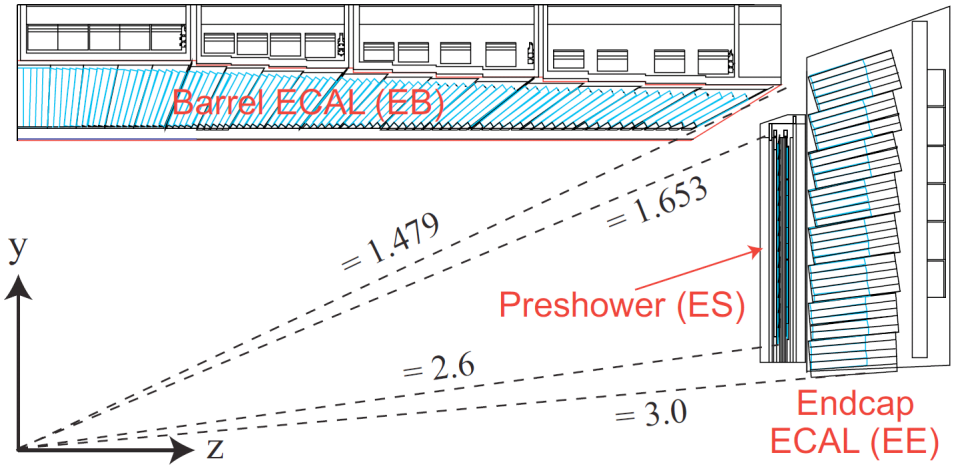

FIGURE II.7: The hadron calorimeter (HCAL). ECAL and trackers also appear at the innermost part.

The inner radius of the barrel 129 cm and covers the pseudorapidity up to $|\eta| = 1.479$.

It consists of 36 supermodules spanning half of the barrel in z direction and 20° in azimuthal direction. The crystals almost point to the nominal interaction point at the center of the detector only by 3° in order to avoid particle trajectories coinciding with the boundary between two crystals, as shown in Figure II.7.

II.2.5 Hadron Calorimeter

The hadron calorimeters (HCAL) are particular for the measurement of hadron jets and neutrinos or exotic particles resulting in apparent missing transverse energy [56]. The absorber material is brass which has a reasonably short radiation length, is easy to process and non-magnetic. The active material consists of plastic scintillators read out with wavelength-shifting fibers.

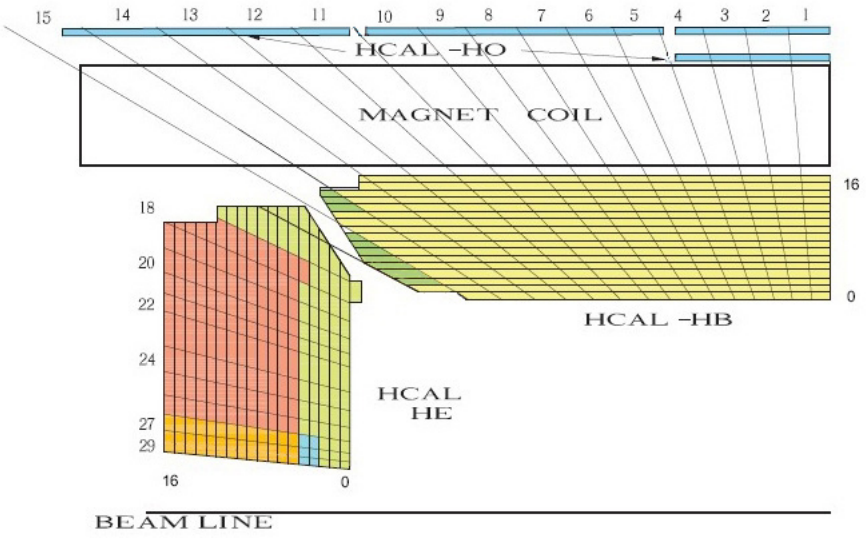

FIGURE II.8: The hadronic calorimeter (HCAL).

The Hadron Barrel (HB) comprises the pseudo-rapidity range up to ±1.4, extending radially from 1.806 m to 2.95 m. On the other hand, the Hadron Endcaps (HE) includes 14 pseudo-rapidity segments each, covering the region 1.3 ¡ $|\eta|$ ¡ 3.0. The Hadron Outer (HO) is placed outside of the solenoid, covering the pseudo-rapidity region ±1.26. The Hadron Forward (HF) calorimeter measures hadrons in the forward region and covers a substantial pseudorapidity range of $|\eta|$ between 3.0 and 5.0, which is important for the measurement of missing transverse energy.

II.2.6 Forward Detectors

The CASTOR (Centauro And STrange Object Research) detector is a quartz-tungsten sampling calorimeter, with characteristics of radiation hardness, fast response and compact dimensions, designed for the very forward rapidity region in heavy ion and proton-proton collisions at the LHC. Its physics motivation is to complement the nucleus-nucleus physics program and also to study the diffractive and low-x physics in pp collisions.

II.2.7 Muon System

Muon detection is a very important tool to recognize signatures of interesting processes over the very high background rate expected at the LHC with full luminosity. An example can be the Standard Model Higgs boson decay in the full leptonic channel $H \to ZZ$ (or $ZZ^{\star}$) $\to 4\ell$, which, in case the leptons are muons, is called "gold plated" channel; or the large variety of Beyond Standard Model theories which predict the presence of muons among the final states. So, precise and robust muon measurement has been a central theme since from CMS earliest design stages.

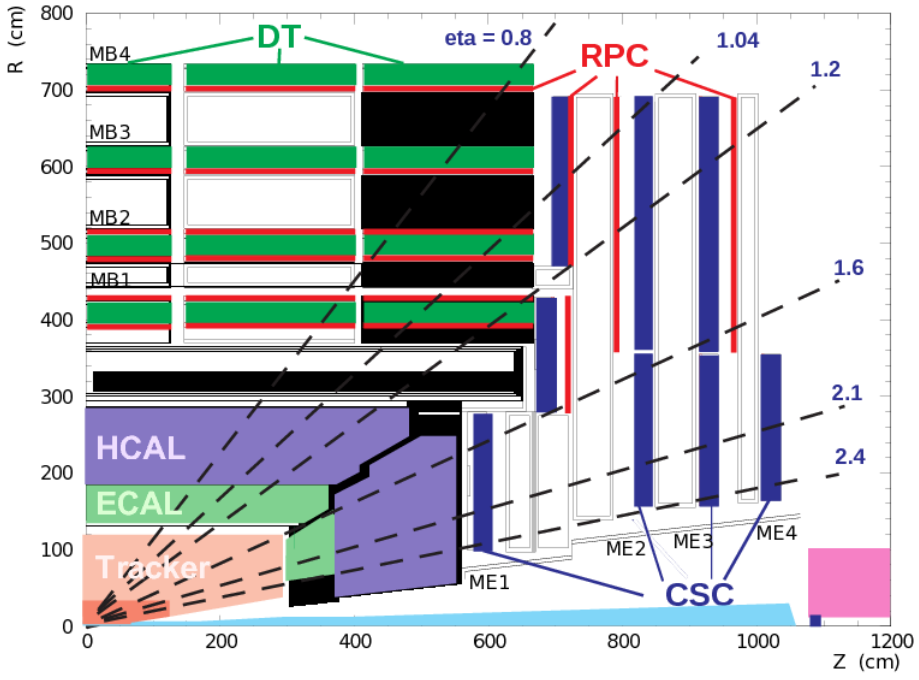

FIGURE II.9: The muon system of the CMS detector.

Three types of gas detectors are used: Drift Tubes (DT), Resistive Plate Chambers (RPC), and Cathode Strip Chambers (CSC), as shown in Figure II.9. Drift tubes are

used in the barrel region, roughly covering $|\eta| < 1.3$, where the particle flux is relatively low. The drift tubes are arranged in chambers MB1 to MB4 at radii of about 4.0, 4.9, 5.9 and 7.0 m, respectively, separated by the iron flux return yoke. The three inner chambers consist of 12 layers of drift tubes, the first and last four measure r and ϕ, while the inner four provide measurements for r and z. The outermost station comprises 14 tube $r - \phi$ measuring layers. The single-point resolution for each tube is about 250 μm, leading to a resolution of 100 μm per chamber and a time resolution of a few nanoseconds. One or two resistive plate chambers are coupled to each DT chamber, which provide additional timing information and allow muon track building at the trigger level.

II.2.8 Trigger

The main challenge for the data taking is the large bunch crossing rate of 40 MHz. To keep the event rate at a manageable level in terms of both storage and computing power requirements, a trigger is used, which selects a subset of events for further storage and processing.

The trigger at CMS consists of two levels. The level-1 trigger reduces the data rate to under 100 kHz. This trigger is implemented using custom hardware and has to reach a trigger decision within 3.2 μs of the bunch crossing. The trigger decision is based on primitive trigger objects, provided by the calorimeter and muon trigger subsystems. Only if the level-1 trigger fires, the event data is read out from the detector.

The event data is zero-suppressed, meaning that only channels with non-vanishing signal are kept, and the remaining data of about 1 MB per event is sent to the surface, where the second level of the trigger decision, the high-level trigger (HLT), is performed. The HLT is implemented in a computing farm running a special version of the CMS reconstruction software. It has around 20 ms CPU time to reach a trigger decision and reduces the trigger rate to under 400 Hz.

Events accepted by the HLT are divided into around 20 primary datasets based on the trigger decision and sent to the Tier-0 computing center at CERN, where a prompt reconstruction is performed within hours of data taking. The recorded data is distributed from the Tier-0 to Tier-1 and further to the smaller Tier-2 computing centers. The main function of the seven Tier-1 centers is the storage, reconstruction, and further distribution of data.

II.3 Reconstruction

In this section it is outlined the reconstruction algorithms applied to the low-level detector response of simulated and recorded events in order to obtain high-level physics objects, such as muons, electrons, jets, and missing transverse energy, which are used to study the underlying interaction.

II.3.1 Particle Flow Algorithm

First approach used at CMS for the reconstruction of jets and missing transverse energy was based simply on the energy deposits measured in the electromagnetic and hadron calorimeters. The energy resolution of these algorithms is limited due to various effects. One of them is that the calorimeter response depends on the particle type and is not perfectly linear in the energy of the particle. Another limitation is that it is assumed that the direction of energy flow associated with a calorimeter tower is given linearly simply extending from the primary vertex towards the position of the measured energy deposit, which is not the case for the charged particles since their trajectories are bent in the magnetic field.

The particle flow (PF) algorithm [57] overcomes some of these limitations by combining track information with calorimeter information, which allows a much better direction resolution and a better energy calibration.

The particle flow algorithm provides particles of five classes, i.e., muons, electrons, photons, charged hadrons, and neutral hadrons. The reconstruction of these particle candidates is based on tracks and calorimeter clusters that are matched using a linking algorithm resulting in blocks. Each of these blocks is classified into one of the five particle categories and an energy correction is applied for each particle candidate.

To convert these blocks into particle flow candidates of one of the five classes, first all muon and electron candidates and the corresponding tracks and clusters are removed. Each of the remaining blocks with a track is classified as charged hadron. The calorimeter energy expected for a charged pion with the momentum given by the track is subtracted from the cluster. Remaining clusters without a linked track are classified as photons, or as neutral hadrons if there is significant contribution of HCAL energy.

The linking algorithm extrapolates tracks to the expected maximum of the energy deposit in the electromagnetic and hadron calorimeter. For electron reconstruction, bremsstrahlung is collected by constructing tangents to the track at tracker layers that are extrapolated to the ECAL. If clusters are found, they are linked to the track. ECAL and HCAL clusters are linked if the ECAL cluster position is within the HCAL cluster envelope. For the muon reconstruction, tracks reconstructed in the inner tracker are matched to track segments reconstructed in the muon system and linked if the global track fit has an acceptable χ^2 value.

II.3.2 Tracking Charged Particles

The tracking reconstruction algorithm [58] combines hits stemming from charged particles traversing the inner tracking system of CMS. The obtained track parameters are used to estimate the momentum of the charged particle at the point of the hard interaction, and the impact parameter[1].

The algorithm begins with the local reconstruction, which matches clusters of the raw detector signals from the pixel detector and the silicon strip detector into hits. For each hit, its position and uncertainty are estimated.

For seeding, two or three hits are combined into pairs and triplets. Each seed provides an initial estimate for the track parameters that are used in the track building step where the current track parameters are used to estimate the position and the uncertainty of the hit position in the next layer, going from the inside to the outside of the CMS tracker. This track propagation accounts for energy loss of the particle in the tracker layers as well. At the next layer, compatible hits are included and the track parameter estimates are updated, iteratively.

Ambiguities may arise if a given track is found by more than one seed or if one seed gives rise to multiple tracks. Therefore, tracks with few hits and large χ^2, which share more than half of the hits with a track with small χ^2, are removed. Finally, the track parameters are re-estimated by a global fit to the track using all assigned hits. This final fit removes any potential bias introduced in the seeding stage.

[1] The impact parameter is the minimum distance from the interaction vertex to the tangent of the track at the point which has the minimum distance from the jet [59].

This track finding algorithm is applied multiple times. This iterative approach allows track finding with reasonable computing time at a high efficiency.

The reconstructed tracks are used to find primary vertices by clustering tracks based on their z coordinate at the closest point to the beam-line. A track can be assigned to multiple clusters with weights based on the compatibility of the track with the z position of the cluster. Then, the vertex positions and uncertainties are estimated from the track clusters.

Primary vertices coming from pile-up interactions usually have few and low-p_{T} tracks. Therefore, the primary vertices are sorted by the decreasing sum of the associated squared track transverse momenta. The first primary vertex after sorting is used as the position of the primary interaction in subject, all other vertices are considered to correspond to pile-up interactions.

II.3.3 Electrons

Electrons traversing the inner tracker can lose a considerable part of their energy by photon radiation at the tracker layers before reaching the electromagnetic calorimeter. These photons are emitted approximately in the current flight direction. This energy loss in the inner tracker is larger for electrons than for other charged particles and the energy in the electromagnetic calorimeter has a large spread in ϕ.

The electron reconstruction algorithm used at CMS starts by searching for clusters in the electromagnetic calorimeter, considering their $\eta - \phi$ asymmetry. Compatible tracks in the inner tracker are searched for these clusters. However, instead of using the track reconstruction algorithm discussed above, a dedicated tracking algorithm is used that accounts for the increased energy loss caused by the photon emissions. The track building uses a Gaussian sum filter to account for the increased energy loss at each tracker layer.

II.3.4 Muons

For the reconstruction of muons, two types of tracks are used. Standalone-muon tracks reconstructed from hits in the muon systems by first searching for short track segments in each muon system and, on the other hand, tracks reconstructed in the inner tracker as described in the charged particle tracking, which are then combined in a track fit.

Two algorithms are used to reconstruct the muon candidates: the global muon reconstruction and the tracker muon reconstruction.

The Global Muon reconstruction propagates the track position both from standalone-muon tracks and the tracks from the inner tracker to a common surface. If they are compatible, a global track is found by fitting a track to all hits used in either one of the tracks.

On the other hand, the Tracker Muon reconstruction begins with tracks reconstructed in the inner tracking system and then extrapolates their position to the muon system, allowing for energy loss as the muon traverses the detector. In the muon system, a compatible track segment is sought.

A muon originating directly from the hard interaction, is successfully reconstructed by both algorithms. In order to supress the rate of such muons from cosmic rays or from the decay of mesons containing c and b quarks, and decay-in-flight muons from decays $K/\pi \rightarrow \mu\nu$ where the track from the kaon is combined with the hits of the muon in the muon chamber, additional identification requirements on the muon candidates are imposed.

One of these requirements is that the global track fit has to fulfill $\chi^2/\mathrm{ndf} < 10$, where ndf is the number of degrees of freedom in the track fit. A minimum number of hits in the inner tracker is imposed as well. These two requirements reject decay-in-flight muons.

Another type of requirement reduces cosmic muon background and muons form heavy flavor decays, that is, the z distance of the muon track extrapolated to the closest approach of the primary vertex has to be smaller than 1 cm and the transverse impact parameter has to be 6 200 μm.

For another requirement, the number of muon chambers with hits used for the track reconstruction has to be at least 2, to be compatible with the requirement of the muon trigger.

II.3.5 Jet Algorithm

The property of QCD known as color confinement implies that quarks and gluons produced in partonic interactions do not remain in a free state, but promptly produce colorless bound states called hadrons. As these hadrons propagate away from the interaction point, they may interact within the detector material, producing additional doughter hadrons. All these processes result as a collimated shower of hadrons known as a jet. In addition to the hard interaction, hadronic activity can result from the underlying event, additional initial and final state radiation, and pile-up interactions. Hadrons are detected as energy depositions in the calorimeter while jets are reconstructed by combining these energy deposits according to a jet definition called anti-k_{T} jet algorithm [60].

Using output from the calorimeter cells, a massless four-momentum k is assigned to each deposition object as follows:

$$k = (E, \vec{p}) \tag{II.4}$$

$$= (p_{\mathrm{T}} \cosh\eta,\ p_{\mathrm{T}} \cos\phi,\ p_{\mathrm{T}} \sin\phi,\ p_{\mathrm{T}} \sinh\eta) \tag{II.5}$$

where ϕ is the azimuthal angle and $\eta = -\ln\tan(\theta/2)$ is the pseudo-rapidity with θ being the angle of a particle relative to the beam axis. Combining two objects is simply adding the two four-momenta as $(E_i + E_j, \vec{p}_i + \vec{p}_j)$.

The anti-k_{T} algorithm needs two distance parameters for some seed object, denoted by an index, that is, d_{ij} is the distance between two seed objects and d_i is the distance between a seed object i and the beam, which are defined respectively as follows:

$$d_{ij} = \min\left(k_{\mathrm{T},i}^{-2}, k_{\mathrm{T},j}^{-2}\right) \frac{\Delta R_{ij}^2}{R^2} \tag{II.6}$$

$$d_i = k_{\mathrm{T},i}^{-2} \tag{II.7}$$

where $R \equiv \sqrt{\eta^2 + \phi^2}$ is the cone radius parameter, $\Delta R_{ij} \equiv \sqrt{(\eta_i - \eta_j)^2 + (\phi_i - \phi_j)^2}$ denotes the angular separation between two objects i and j, and $k_{\mathrm{T},i}$ is the transverse momentum of the object i.

The algorithm starts with some seed object and then calculates the distance parameters between the seed and other objects to be combined. If the shortest distance is a two-obejct distance, d_{ij}, objects i and j are combined and the algorithm proceeds with the

newly combined object as a seed. If a beam distance, d_i, is the shortest distance, the object is called a jet and removed from the list of entities to be combined. A new seed is then selected and the process proceeds until no object remains.

II.3.6 Missing Energy

Some particles such as neutrinos in the Standard Model, or certain hypothetical particles in theories beyond the Standard Model, escape the detector without leaving any signal that could be used for a direct detection. However, such particles can be detected indirectly as they show an imbalance in the total momentum of the final state compared to the initial state.

This principle can only be applied to the transverse momentum, as the proton remnants leave the detector in the beam line. Therefore, the missing transverse energy is the momentum vector in the x-y plane that restores the momentum balance, given by the following:

$$\vec{\not{E}}_{\mathrm{T}} = -\sum_i \vec{p}_{\mathrm{T},i} \tag{II.8}$$

where i runs over all final state objects, i.e., particle flow candidates. The magnitude of the vector $\vec{\not{E}}_{\mathrm{T}}$ is denoted with $\not{E}_{\mathrm{T}}$ which is a useful quantity to distinguish between processes with and without neutrinos in the final state.

Chapter III

The Analysis: Single Top-Quark Cross-Section Measurement using Multivariate Techniques

This chapter presents a multivariate analysis of the measurement of the cross-section of the single-top quark in s-channel produced from the proton-proton collisions where the collision data are provided by the LHC and recorded by CMS in 2012, with the luminosity of 19.3 fb^{-1} having an uncertainty of 2.5%, at a centre-of-mass energy of $\sqrt{s} = 8$ TeV.

The aim of the work is to optimize the choice of the input variables used in the multivariate technique for the cross-section measurement of the single top-quark production and understand the correlations between physical entities for the event topology in subject, i.e. s-channel. For the optimization process, an iterative feedback mechanism is introduced and the data from the Monte Carlo simulations are used to test the discrimination of each iteration.

The strategy of the analysis is to extract a distribution of a multivariate discriminator to seperate single-top quark events from its main background contributions. The multivariate technique used in this analysis is based on Boosted Decision Trees (BDT) which is a method to combine a sort of variables into a single variable by assigning weights to each event and evaluating the correlations among these variables for the given data. The use of BDT method in this study is discussed in Section III.4 in details.

As discussed in Section I.2.2, the s-channel topology consists of the interaction of a quark and an anti-quark with distinct flavour producing a W-boson which decays into a top quark and an anti-bottom quark as predicted by the Standard Model. Since the top quark decays into bottom quark quickly before it could interact with the calorimeters of the detector, the final state of the collision expected to give two bottom or anti-bottom quark signature, one from top quark and one, of opposite flavour, directly from the W-boson decay. The signature of a (anti-)bottom quark is actually not a bare quark, but rather a shower of particles emerged from the interaction of the quark and the detector rising to several mesons and hadrons, and called a jet (see Section II.3.5), or specifically a b-jet if it comes from a bottom or anti-bottom quark, respectively.

In order to perform such an analysis, one expectingly starts with the reconstruction of the particles as explained in Section II.3 and the selection of the events as elaborated in the first section of this chapter. The following section is about the control samples and background processes. Then in the Section III.4, the method of Boosted Decision Trees is discussed with how the variables are determined, followed by a section for the Testing and Training of the output.

The topology of the s-channel and its small production cross section with respect to the huge background processes (as $t\bar{t}$) lead to fulfil the analysis with choosing a multiple set of variables and extract one combination of those which has the best discriminating power regarding to the tests and trainings of the Monte Carlo samples, as it is discussed in full details in Section III.4.1.

As a consequence of the statistical model followed in this thesis, the extraction of the cross-section measurements are our final results.

In Section III.4.3, it is presented the statistical model adopted for the cross-section measurement. In the end of the study, single top-quark production is measured and the results are manifested in the last section of the chapter.

III.1 Event Selection and Reconstruction

The final-state topology for the single-top production in the the s-channel is given by exactly one isolated muon or electron, and two b-quarks, one from the top-quark decay

and one recoiling against the top quark. Therefore the event selection have been optimised as in the published analysis [48] by requiring p_{T} and $|\eta|$ cuts with High-Level Trigger and online track-based isolation, as explained below.

III.1.1 Primary Vertex, Noise Cleaning and Triggers

It is required at least one primary vertex to be reconstructed from at least four tracks, constaining the track fit to have 5 numbers of degrees of freedom, with $|z_{\mathrm{PV}}| < 24$ cm and $\rho_{\mathrm{PV}} < 2$ cm, where $|z_{\mathrm{PV}}|$ and ρ_{PV} are the vertex distance with respect to the nominal interaction point along the z-axis, and in the transverse plane respectively.

For noise cleaning, events with very high energy noise in the HCAL barrel or endcaps are rejected, using pulse shape, hit multiplicity, and timing criteria.

Muon events are selected using the the High Level Trigger requirement which selects muon candidates with $p_T > 24$ GeV/c and $|\eta| < 2.1$ during the online reconstruction.

Electron events are selected using the High Level Trigger requirement where the efficiency for prompt electrons with $E_T > 27$ GeV have a nominal value of 80%.

III.1.2 Electrons and Muons

As discussed in Section II.3.3, an electron is detected as a track ending with a cone of energy deposits in the electromagnetic calorimeter, which consist of charged or neutral hadrons and photons, since the lepton yields these particles to be created when it interacts with the media of the calorimeter. On the other hand, a muon is detected among the four layers of muon stations consist of chambers which sit outside the magnet coil, as explained in Section II.3.4.

A lepton signature should be seperated from any other particle shower activity like jets defined in the next subsection. Therefore, in order to isolate a lepton in the terms of these particles, one needs to define such a variable called “relative isolation”, as detailed below.

The relative isolation of a lepton is defined by the ratio between the sum of the transverse energies of the photons, charged hadrons and neutral hadrons in a cone of the size $\Delta R = \sqrt{(\Delta\eta)^2 + (\Delta\phi)^2}$ around the lepton direction, and the transverse momentum of

the lepton. Explicitly,

$$I_{\text{rel}} \equiv \frac{E_{\text{T}}^{\text{PF,C.Had.}} + \max\left(E_{\text{T}}^{\text{PF},\gamma} + E_{\text{T}}^{\text{PF,N.Had.}} - \Delta\beta,\, 0\right)}{p_{\text{T}}\, c} \tag{III.1}$$

where p_{T} is the transverse momentum of the lepton and E_{T}^{PF} is the sum of the energy bins deposited in the transverse plane associated by the particle-flow algorithm to the photons, charged hadrons and neutral hadrons, respectively. Here the abbriviation $\Delta\beta$ is a correction term defined according to which the lepton is a muon or electron, as follows.

In the case of an electron $\Delta\beta \equiv \rho\, A$ where ρ is the avarage energy of the particles not used to reconstruct jets, and A is the effective area of the jet cone in the $\eta - \phi$ plane. On the other hand, for muons $\Delta\beta \equiv 0.5 \sum p_{\text{T}}^{\text{PU}}$ where p_{T}^{PU} is the tranverse momentum of the tracks associated to non-leading vertices, used to estimate the contribution of neutral particles from pileup events. The factor 0.5 is to take into account the neutral-to-charged particles ratio expected from isospin invariance.

Therefore, electrons are isolated inside a cone of the size $\Delta R = 0.4$ with $I_{\text{rel}} < 0.1$ and selected by the cut of $p_{\text{T}} > 27$ GeV/c and $|\eta| < 2.5$. The ECAL barrel-endcap transition region with $|\eta|$ of the supercluster between 1.4442 and 1.5660 is excluded from the selection for electrons.

On the other hand, muons are isolated inside a cone of the size $\Delta R = 0.3$ with $I_{\text{rel}} < 0.12$ and selected by requiring $p_{\text{T}} > 24$ GeV/c and $|\eta| < 2.1$.

For a further veto of the leptons, it is also defined a loose criteria which loosens the requirement to $E_{\text{T}} > 20$ GeV/c for electrons, and $I_{\text{rel}} < 0.2$ with $p_{\text{T}} > 10$ GeV/c and $|\eta| < 2.5$ for muons, respectively.

III.1.3 Jets

A jet is an object consisting a narrow cone, or namely shower, of hadrons stemming from a gluon or a quark clumping to form groups such as mesons or hadrons, since particles carrying a colour charge can not be isolated singularly because of the QCD confinement. This phenomenon which is called hadronization prevents one to observe a quark or a gluon in the detectors, but instead leads to the detection of a plenty of particles which could be associated to each other wihin a cone in the $\eta - \phi$ plane.

Jets are reconstructed using the anti-k_T algorithm, introduced in Section II.3.5, with a cone size of $R = 0.5$, taking the particles identified by the Particle Flow (PF) algorithm (see Section II.3.1) as input. The jet energy is scaled by a factor which describes the detector response depending on the transverse energy and the pseudorapidity of the jet.

Charged particle candidates not associated to the main primary vertex are subtracted from the event in order to reduce contamination from the pile-up events. The energy of the jet is then corrected by the amount of energy deposited by neutral pile-up hadrons in the jet area. The analysis considers jets within $|\eta| < 4.5$. The transverse momentum for the two most energetic jets is required to be greater than 40 GeV/c, while other jets in the events are considered in the analysis if they have at least 30 GeV/c.

III.1.4 Missing transverse energy and W-boson transverse mass

Missing transverse energy is defined the opposite of the vectorial sum of the transverse momenta of the identified Particle Flow (PF) particles. The transverse mass is defined as follows:

$$m_T = \sqrt{(p_{T,\ell} + p_{T,\nu})^2 - (p_{x,\ell} + p_{x,\nu})^2 - (p_{y,\ell} + p_{y,\nu})^2} \quad \text{(III.2)}$$

where the transverse momentum components of the neutrino are approximated by the components of the missing transverse energy vector, $\vec{\not\!\!E}_T$.

In order to estimate the contribution of processes where the lepton does not come from a leptonically decaying W boson, a fit is performed to the distributions of the transverse W-boson mass m_T in the muon channel and a fit to the $\not\!\!E_T$ in the electron channel, as it is detailed in Sec. III.2.

We assume that the x and y components of the missing energy are entirely due to the escaping neutrino, and apply the W-mass constraint in order to extract the z component.

$$m_W^2 = \left(E_\ell + \sqrt{\not\!\!E_T^2 + p_{z,\ell}^2}\right)^2 - \left(\vec{p}_{T,\ell} + \vec{\not\!\!E}_T^{\,2}\right)^2 - (p_{z,\ell} + p_{z,\nu})^2 \quad \text{(III.3)}$$

This equation has two solutions for $p_{z,\nu}$ as follows:

$$p_{z,\nu}^{\pm} = \frac{\Lambda\, p_{z,\ell}}{p_{T,\ell}^2} \pm \sqrt{\frac{\Lambda^2\, p_{z,\ell}^2}{p_{T,\ell}^4} - \frac{E_\ell^2\, \not\!\!E_T^2 - \Lambda^2}{p_{T,\ell}^2}} \quad \text{(III.4)}$$

where $\Lambda \equiv \frac{1}{2}m_W^2 + \vec{p}_{T,\ell} \cdot \vec{\not{E}}_T$.

Due to a finite $\not{E}_T$ resolution, in the 36% of the cases, the discriminant in Eq. (III.4) becomes negative, which is equavalent to $m_T > m_W$, making the solutions imaginary. Several schemes have been used to deal with this situation. In this analysis, the imaginary component is eliminated by modifying $\not{E}_T$ such to give $m_T = m_W$ and thus the discriminant to be null, still respecting the constraing in Eq. (III.3). This condition implies a quadratic relation between the transverse components of the momenta of the neutrino, with two solutions amoung which the one with minimal distance $p_{T,\nu}$ and $\not{E}_T$ is choosen. In the case of two real solutions for $p_{z,\nu}$, the one with the smallest absolute value is choosen in this analysis.

III.1.5 *b*-tagging and mistagging

In order to identify the jet springing from *b*-quark, the "track counting" in the "high purity" version (TCHP) is used, among several *b*-tagging algorithms available in CMS. This algorithm calculates the signed 3D impact parameter significance ($\mathrm{IP}/\sigma_{\mathrm{IP}}$) of all the tracks associated to the jet that passes tight quality criteria, then orders them by decreasing values of this observable, and finally outputs as jet discriminator the value of $\mathrm{IP}/\sigma_{\mathrm{IP}}$ for the third ($D_T CHP$) track. Jets which pass the tight threshold of this discriminator are considered as originated from *b*-quarks.

The data/simulation scale factors and corresponding uncertainties on efficiencies and mistagging rates have been evaluated within the CMS collaboration. These scale factors have been applied to the analysis, and their uncertainty is taken into account as contribution to the systematic uncertainty.

The signature of single-top production in the s channel includes two partons in the final state, that is, first *b* quark recoiling against the top, and second *b* quark comes from the top-quark decay. From now on, it will be used the notation "n-jets m-tags" to refer to a sample that has n reconstructed jets, m of which pass the *b*-tag threshold. Notable samples which are studied and used in this analysis are the 2-jets 0-tags sample (W+jets enriched), the 2-jets 2-tags (s-channel enriched) and the 3-jets 2-tags (enriched with $\mathrm{t\bar{t}}$ events).

III.1.6 Top quark

Since the top quark decays into a lepton, a b-jet and a neutrino, it could be recognized by the peak in the spectrum of the invariant mass of these objects.

All top-quark decay products are reconstructed in the detector, except for the neutrino which remains invisible. While the transverse momentum of the neutrino can be deduced from the missing energy, the longitudinal momentum can be determined from an extra assumption, namely the W-mass constraint explained in Sec. (III.1.4).

Due to presence of two b-tagged jets in final state of s channel, there is a possibility to associate a wrong b-jet to the lepton when performing the top-quark reconstruction. In order to decrease the fraction of events with wrong assignment, an approach which compares the top masses reconstructed for each b-jet with the nominal top mass is used to choose the b-jet for top reconstruction.

First of all, it is reconstructed two top masses with each b-jet, and then the one which has minimal distance with respect to nominal top mass used in the Monte Carlo generator (172.5 GeV/c^2) is chosen. Henceforth, this will be refered as "best-mass-top" method. The efficiency of association of true b-jet quark to the top is 76% (74%) in s channel anti-top, 73% (73%) in s channel top and 70% (70%) for $t\bar{t}$, in the electron (muon) channel. The dependency of the correct b-jet association on the top mass has been evaluated in s-channel events by varying the top mass by 1.5 GeV/c^2, and resulting in an efficiency variation of less than 1%.

The performances of a different top reconstruction method based on a likelihood ratio is tested as well. The method is set up making use of three variables discriminating the b-jet coming from top-quark and b-jet recoiling against the top: $p_{\mathrm{T},b}$, $M_{\ell b}$ and η_b, where $p_{\mathrm{T},b}$ is the b-jet transverse momentum, $M_{\ell b}$ is the invariant mass of the lepton and b-jet system, and η_b is the pseudo-rapidity of the b-jet.

The b-jet which has larger likelihood ratio is taken as the b-jet from top decay. At the end the efficiency of b-jet to top association is 73.4%, 73.5% for s-channel top production and 73.1% for s channel anti-top, in the muon channel. The top-quark reconstructed in the way explained above is refered as "LR-top".

The angular distribution of the lepton is yet another useful feature that could benefit from the reconstruction of the top-quark, since it is related with the top-quark polarization which presents a specific feature of the electroweak single-top production mode in the s channel. We define $\cos\theta^{\star}$ and $\cos\theta_{\ell j}$ as the cosine of the angles between the lepton and the beam axis and the direction of the jet which recoiled against top-quark, respectively, in the top-quark reconstructed rest frame.

III.2 Control Samples and Data-driven Background Estimations

To seperate the single top-quark signal from its main backgrounds, the samples are modeled in several categories according to how many of the jets are b-tagged as explained in Sec. (III.1.5). So, the modeling of the most important background processes has been studied in control samples orthogonal to the signal-enriched sample, namely, 2-jets 2-tags. The W+jets is validated in the 2-jets 0-tags sample, while the 3-jets 2-tags sample is studied to validate the $t\bar{t}$ model for the signal region.

Due to the low statistics and to their negligible contribution as backgrounds, diboson backgrounds (WW and ZZ) were not taken into account in the analysis. The remaining categories such as 3-jets 0-tags or 4-jets m-tags are not included in the analysis since they lack any significant signal/background seperation.

III.2.1 Vector Bosons + jets

Since the 2-jets 0-tags sample is enriched in W + light flavoured jets, while in the 2-jets 2-tags signal sample the W + heavy flavours component is dominant, this sample has not been used to constrain the W+jets background in the signal cross-section extraction, but only to provide an additional check of overall data/MC agreement.

III.2.2 Top-antitop

To obtain a data sample enriched in $t\bar{t}$ events we require the presence of 3 jets, two of which must satisfy the b-tagging requirements (3-jets 2-tags). This category is particularly important since $t\bar{t}$ production is the main background to the single-top s-channel

process in the signal enriched sample. The top-quark reconstruction is performed as described at the end of Sec. (III.1.6), with "best-mass-top" hypothesis for electrons and muons. This sample is used in the final signal extraction procedure together with the signal-enriched 2-jets 2-tags sample, and allows to put a constrain on the $t\bar{t}$ overall contribution.

III.2.3 QCD Background Estimation

The event yield of multijet QCD events in signal and control samples is estimated performing a fit to the distributions of the transverse W-boson mass $m_{\mathrm{T}W}$ in the muon channel as shown in Figure III.1, and a fit to the $\not\!\!E_{\mathrm{T}}$ in the electron channel.

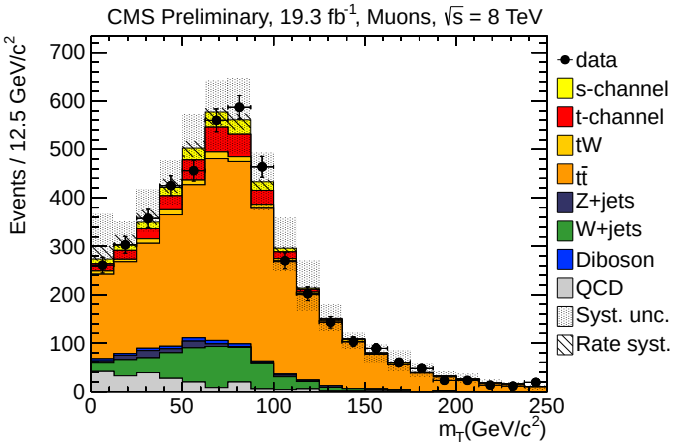

FIGURE III.1: Transverse mass of the W boson in 2J2T category for the muon channel.

III.3 Systematic Uncertainties

This section describes the sources of systematic uncertainty which can affect the measurement of the single-top cross section in the s channel in the 2-jets 2-tags event category. We consider three families of such uncertainties: those affecting the background rates, instrumental and theoretical ones.

III.3.1 Background Normalisation

It has been assigned 10% and 30% to $t\bar{t}$ and W+jets the uncertainties coming from the CMS measurments, respectively. The QCD uncertainty is taken from the extraction procedure described in Sec. (III.2.3) and corresponds to 30% (25%) for muons in the 2-jets (3-jets) 2-tags category and 21% (10%) for electrons in 2-jets (3-jets) 2-tags category (respectively). For the remaining backgrounds, motivated by theoretical and experimental uncertainties, we use ±30% for dibosons, ±15% and ±20% for single top t-channel and tW-associated production, and 20% for Z+jets.

III.3.2 Instrumental Uncertainties

- **Jet Energy Scale.** The uncertainty on the jet energy scale (JES) is taken from the official CMS jet energy corrections (JEC), available in the conditions database, with the global tag `GR_R_53_V27`. For each variation the $\not\!\!E_{\mathrm{T}}$ is recalculated accordingly.

- **Unclustered $\not\!\!E_{\mathrm{T}}$.** A shift of ±10% on the "unclustered energy" component of the $\not\!\!E_{\mathrm{T}}$ is taken into account. The unclustered energy is defined by subtracting the uncorrected four-momenta of all jets from the event and the four-momenta of all leptons not clustered in jets. Then the $\not\!\!E_{\mathrm{T}}$ is recalculated and the corresponding shift is propagated to the measurement.

- **Jet Energy Resolution.** A smearing is applied to account for the known difference in jet energy resolution with respect to data, increasing and decreasing the extra resolution contribution by its uncertainty.

- **Lepton trigger and reconstruction.** The uncertainty on the lepton reconstruction and trigger efficiencies scale factors are measured from Drell-Yan events. An additional uncertainty of 3% in the muon channel is considered to account for the uncertainty due to the I_{rel} cut.

- **b-tagging and mis-tagging.** The scale factors used to correct for the different efficiencies in data and Monte Carlo are varied independently according to measured uncertainties and applied according to the prescriptions quoted in [61].

- **Pile-up.** The number of pile-up events depends on the total inelastic pp cross-section at LHC. The uncertainty on this cross section, 5%, is used to obtain $\pm 1\sigma$

variated distributions of number of true pile-up events in data. The simulated pile-up events are reweighted according to these modified distributions and the impact on the measurement is evaluated.

- **Luminosity.** The luminosity is known within 2.6% uncertainty.

III.3.3 Theoretical Uncertainties

- **Factorization and renormalization scales, Q^2.** Dedicated simulated samples with renormalization and factorization scales μ_R and μ_F varied from half to twice their nominal value are used for $t\bar{t}$, W+jets, and single-top t-channel and s-channel.
- **Matrix element and Parton shower matching thresholds.** dedicated simulated samples with matching threshold doubled and halved are used for $t\bar{t}$ and W+jets samples.
- **Parton Distribution Functions.** The uncertainty due to the choice of the set of parton distribution functions (PDF) is estimated using pseudo-experiments, reweighting the simulated events with each of the 52 eigenvectors of the `CT10`, and repeating the nominal signal extraction procedure. For the reweighting of the simulated events, the `LHAPDF` [62] package is used.
- **Top p_{T} reweighting.** The differences between the top quark p_{T} observed in data and generated in simulation are taken into account as a systematic uncertainty.
- **Simulation Uncertainties** The effect of the limited amount of statistics in the simulated samples has been considered as well as additional systematic uncertainty.

III.4 BDT Discriminant

The Standard Model prediction for single top-quark production via the s channel at the LHC is very small with respect to its main backgrounds like $t\bar{t}$ or t channel. The s channel is not suitable for analyses with one single variables but rahter one needs to exploit a combination of several variables.

For this reason, it has been chosen to profit from as much discriminating power as possible through a multivariate classification approach. The “Toolkit for Multivariate Analysis” (TMVA) [63] is used for evaluation, test and application of classification.

Option	Value	
`NTrees`	400	Number of trees in the forest
`BoostType`	AdaBoost	Boost type
`PruneMethod`	CostComplexity	Method of pruning
`SeparationType`	GiniIndex	Separation criterion for node splitting
`MaxDepth`	2	Maximum depth of the decision tree allowed
`PruningValFraction`	0.25	Fraction of events to use for optimizing automatic pruning
`PruneStrength`	-1	Pruning strength is set to be determined by TMVA

TABLE III.1: The options used for the BDT method in this analysis.

The method of Boosted Decision Trees is a machine learning algorithm that builds up a classification tree where leaves represent class labels and branches represent logical conjunctions of features that lead to those class labels. The goal of this method is to create a model that predicts the value of a target variable based on several input variables.

Decision tree are sensitive to statistical fluctuations of the training sample. In order to make it more robust, boosting methods are recommended. Boosting is a general method of creating a collection of classifiers instead of one, which can be combined to make a new classifier more stable and with smaller misclassification probability. Adaptive boosting algorithm calculates the boost weight that will be used in the next tree, depending on the number of misclassified training events in the previously growned tree. It gives a higher weight to an event if it was classified incorrectly in the past. Generating new trees will continue until a certain number of `NTrees` set by the user is reached.

BDTs are in general sensitive to overtraining, in the sense that when classifiers are too much adapted to a specific training sample, similar samples can have a completely different response from the trained classifier. It means one can not rely on the BDT output for real data, which will be classified different from the training sample. Different methods called "pruning" have been adopted to deal with this problem. Pruning is just cutting down the leaf-nodes which are statistically insignificant. For BDTs, it's available for `AdaBoost` with two methods: `CostComplexity` and `ExpectedError`. The strength of the pruning is controlled in TMVA with the parameter `PruneStrength`, which can either be optimized by TMVA or determined by user.

III.4.1 Determining Variables

In this section, the variables are introduced briefly. In order to determine which variables are chosen to be used in the multivariate analysis, a feedback method seeking for the most discriminant ones is explained in details. The distributions of each variable for the muonic final state is given both for 2-jets 2-tags and for 3-jets 2-tags categories, with signal being blue and background being red.

- m_{T}, Transverse W boson mass. This variable keeps track of the lepton and neutrino momenta as well as their angular correlation, presenting a clear Jacobian peak for lepton-neutrino pairs stemming from a W-boson decay. This variable proves to have a significant discriminating power between events where a single W-boson is produced, like for instance in s-channel events, and events where there are two or no W-bosons at all. The $\mathrm{t\bar{t}}$ events where both tops decay through the leptonc decay chain ascribe to the first category, while multijet QCD events are of the second type.

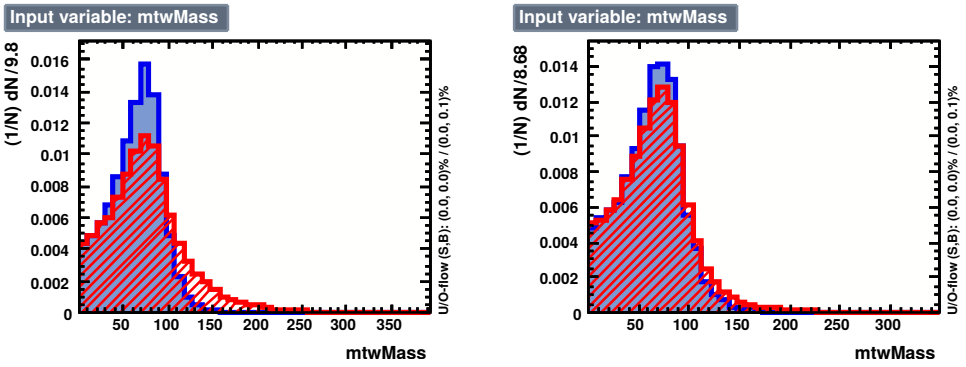

(A) 2J 2T category (B) 3J 2T category

FIGURE III.2: Transverse mass of the W boson for the muon channel.

- $\Delta\Phi_{\mathrm{top,bJetRecoil}}$, difference in azimuthal angle between top quark and recoiled b-tagged jet. The top and recoil b-quark are produced almost back-to-back in the CMS reference frame for signal events, while such is not the case in $\mathrm{t\bar{t}}$ events for one of the top quarks and the b-quark from the decay of the other. Albeit this effect is mitigated by the b-jet to reconstructed top association efficiency, it results in the discriminating power of the the angular separation variables between reconstructed tops and the recoiled b-jet. The use of this variable reduces the dependency on the assumption made to derive the longitudinal component on the neutrino for the top reconstruction.

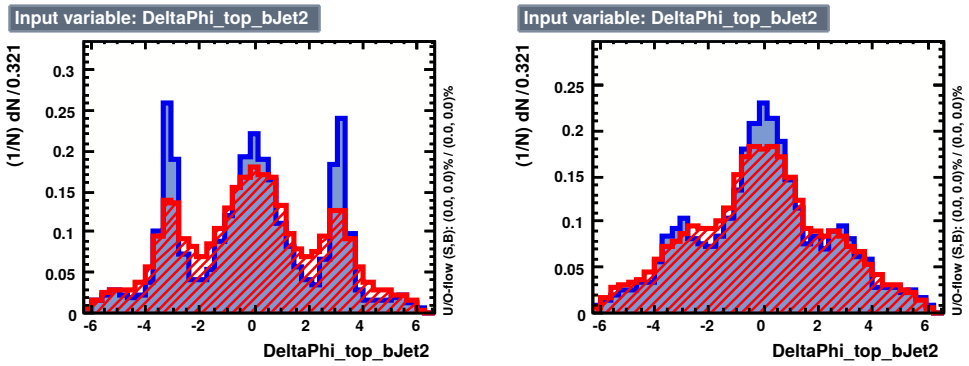

(A) 2J 2T category (B) 3J 2T category

FIGURE III.3: The difference in azimuthal angle between top quark and recoiled b-tagged jet for the muon channel.

- p_{T}^{ℓ}, transverse momentum of the lepton.

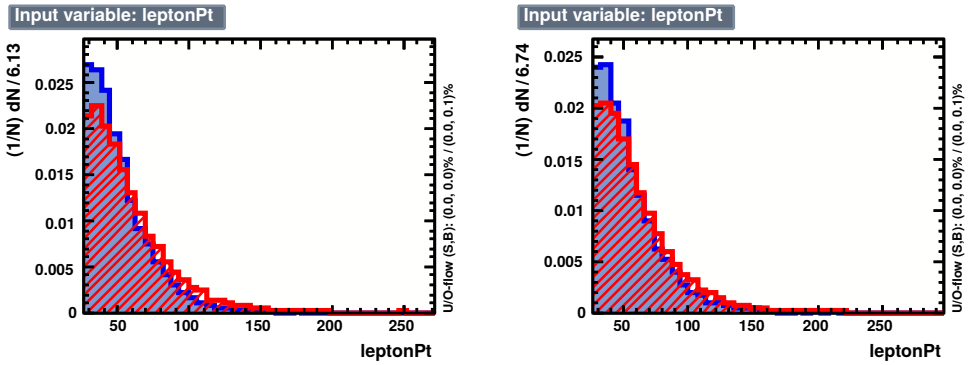

(A) 2J 2T category (B) 3J 2T category

FIGURE III.4: Transverse momentum of the muon channel.

- $\not\!\!E_{\mathrm{T}}$, missing transverse energy. The p_{T} spectrum of the lepton and the neutrino from the W-boson decay are different for signal and the main backgrounds in particular being softer for the signal and harder for $\mathrm{t\bar{t}}$ where additionally the $\not\!\!E_{\mathrm{T}}$ is increased by the presence of an extra neutrino in the case of dileptonic events.

- $M_{\ell b1}$, invariant mass of the lepton and the leading b-tagged jet.

- $M_{\ell b2}$, invariant mass of the lepton and the second-to-leading b-tagged jet. This constraints the distribution of their invariant mass, while in case of wrong b-jet association, or if a top-quark is not present in the event, such distribution is broader. In general, for the s channel the spectator b has higher momentum, while for $\mathrm{t\bar{t}}$ events the spectra of the b-quarks are identical and for the t-channel

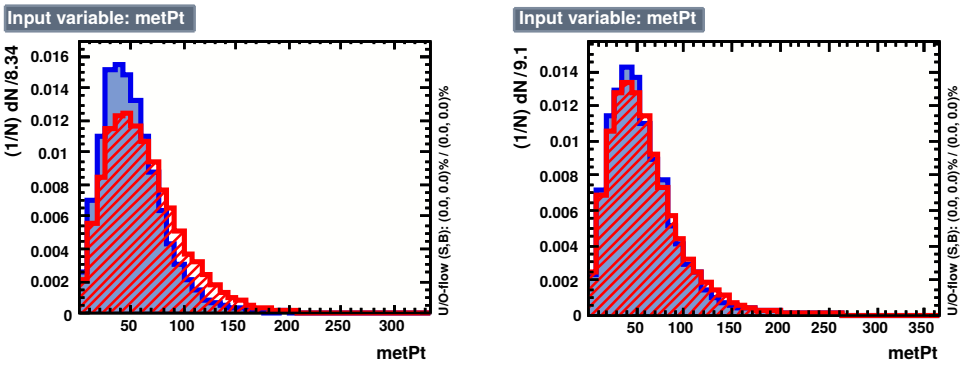

(A) 2J 2T category (B) 3J 2T category

FIGURE III.5: Missing transverse energy for the muon channel.

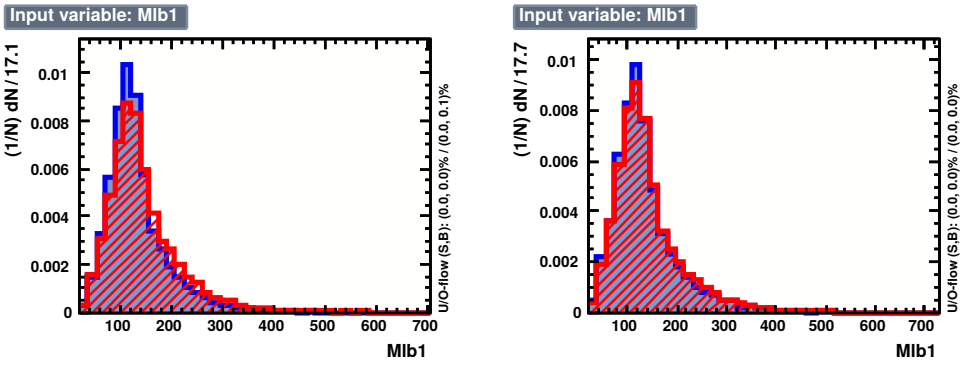

(A) 2J 2T category (B) 3J 2T category

FIGURE III.6: Invariant mass of the lepton and the second-to-leading b-tagged jet.

the spectator b is softer instead. Thus the invariant mass between the second-to-leading b-jet and the lepton presents a sharper peak for the signal, and a broader distribution for the backgrounds.

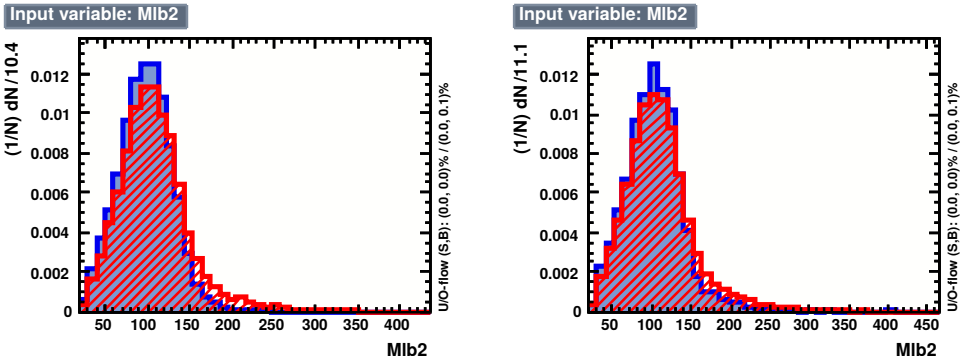

(A) 2J 2T category (B) 3J 2T category

FIGURE III.7: Invariant mass of the lepton and the second-to-leading b-tagged jet.

- $\cos\theta_{\ell j}$, cosine of the angle between the lepton and the beam axis in top-quark rest frame, and $\cos\theta^{\star}$, cosine of the angle between the lepton and the b-tagged jet

recoiling against the top quark, in the top-quark rest frame. The distribution of the latter variable in s-channel signal events stems from the left(right) polarisation of the single-top-quark(anti-quark), which is itself a consequence of the V-A nature of the electroweak interaction. By converse, top quarks from $t\bar{t}$ processes are produced unpolarised and W+jets events, having a completely different topology, inherit the shape of those variables from the angular correlations between the W and jets.

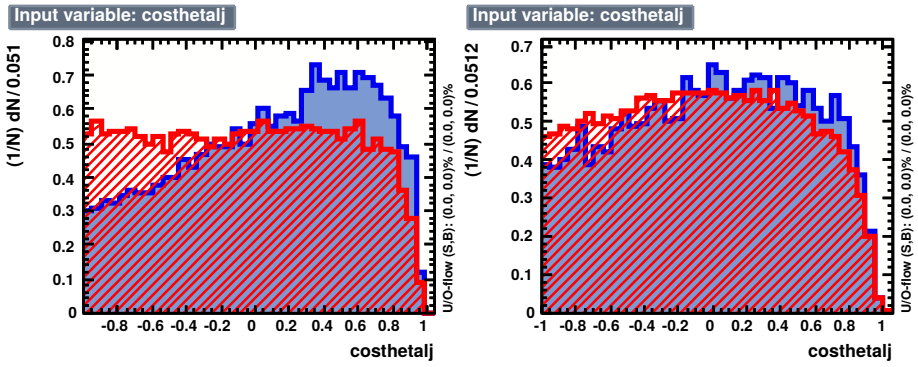

FIGURE III.8: Cosine of the angle between the lepton and the b-tagged jet recoiling against the top quark.

- p_{T}^{bb}, vector sum of p_T of the two b-tagged jets. The two b-jets stemming from the $t\bar{t}$ pair decays or W+jets associated production show to have a harder spectrum with respect to the signal events, as the bb pair in signal events carries a larger fraction of the original transverse momentum of the system, peaking around zero.

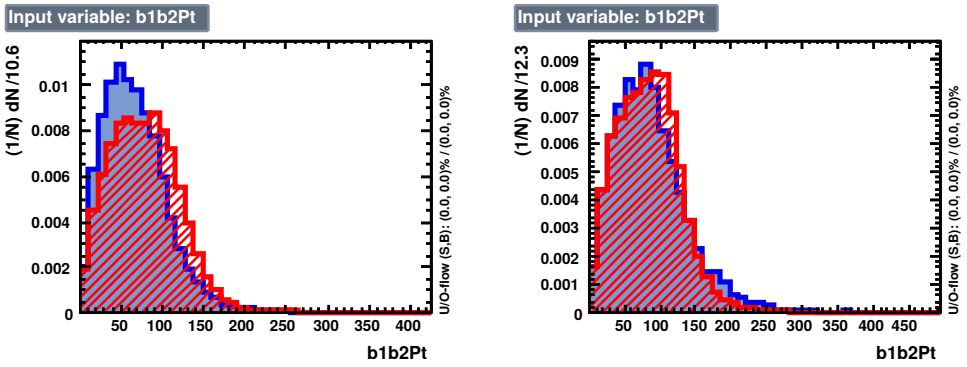

(A) 2J 2T category (B) 3J 2T category

FIGURE III.9: Vector sum of p_T of the two b-tagged jets.

- $M_{\ell b\nu}$, invariant mass of lepton, neutrino and one of the b-tagged jets reconstructed with the best-mass top method.

- $\Delta R_{b'\ell}$ and ΔR_{bb}: The angular separation between the b-tagged jet recoiling against the top quark and the lepton, and the angular separation between the two b-tagged jets. As for the angular separation between the top-quark and the recoil b-jet, also the angular separation of the top decay products, the lepton and the b-quark, yields a good discriminating power between the s-channel and its backgrounds. Since there's no ambiguity in the definition of the lepton and b-jet η, as it is instead the case for the reconstructed top-quark, one can exploit this information to use as discriminating variable the distance in the $\eta - \phi$ plane as opposed to the simple difference in ϕ as for the top-quark.

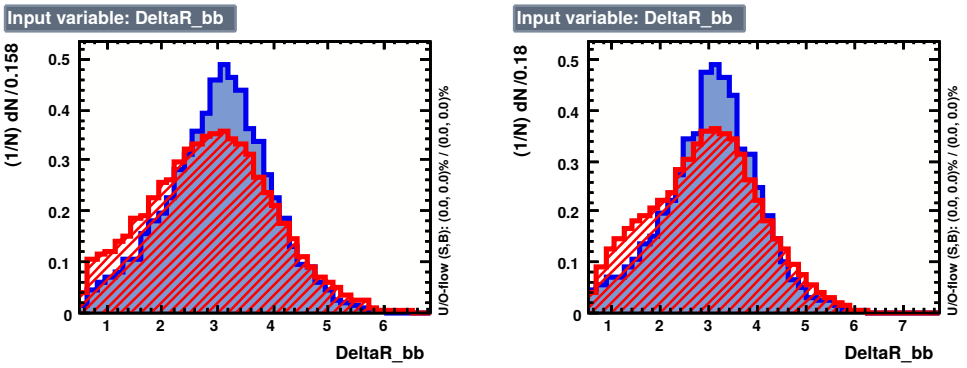

(A) 2J 2T category (B) 3J 2T category

FIGURE III.10: The angular separation between the b-tagged jet recoiling against the top quark and the lepton.

- H_{T}, scalar sum of p_T of all jets.Signal events produce a relatively jet-clean environment, involving the production of only two b partons in the hard scattering, while for instance $\mathrm{t\bar{t}}$ semileptonic events foresee the presence of at least two extra partons. Also, in general $\mathrm{t\bar{t}}$ events are produced with higher jet multiplicity due to the presence of two hard gluons in the final state. Thus the total scalar sum of the jets energy provides a good discriminating power between signal and $\mathrm{t\bar{t}}$ in particular.

- η, pseudorapidity of the high p_T jet.

- M_{b1b2}, invariant mass of the leading and the second-to-leading b-tagged jet.

- $p_{\mathrm{T}}^{\mathrm{loose}}$, transverse momentum of the loosely selected jet.

- m_t-best, mass of the top quark obtained with best-top method.Reconstructed top mass is a powerful discriminant with respect to W+jets and backgrounds that do not contain a top quark, presenting a clear peak structure for signal events.

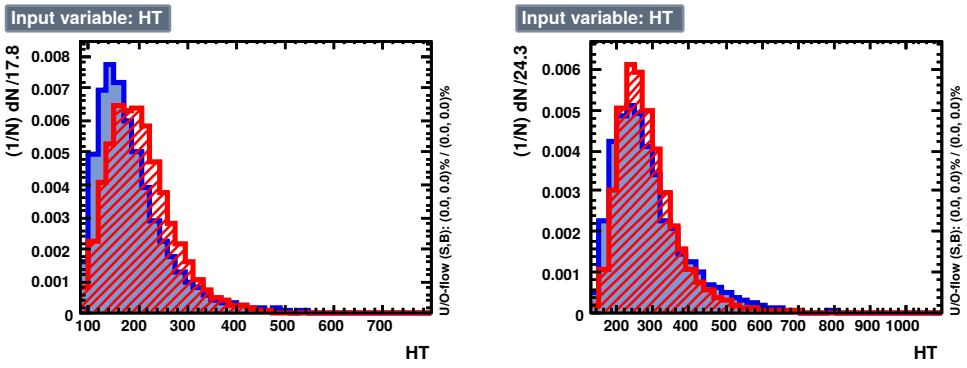

(A) 2J 2T category (B) 3J 2T category

FIGURE III.11: Scalar sum of p_T of all jets.

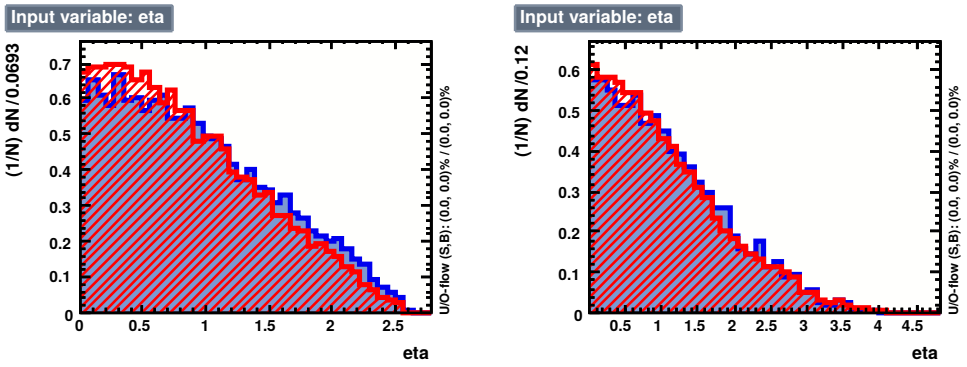

(A) 2J 2T category (B) 3J 2T category

FIGURE III.12: The pseudorapidity.

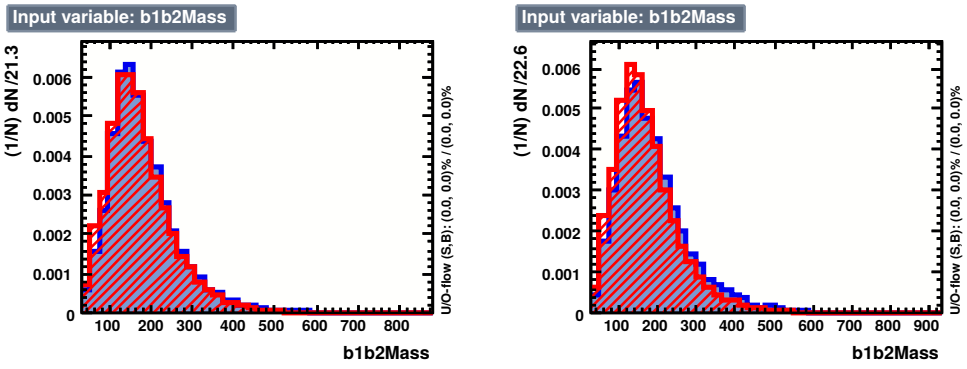

(A) 2J 2T category (B) 3J 2T category

FIGURE III.13: Invariant mass of the leading and the second-to-leading b-tagged jet.

As some of the above variables describe the same physical quantities for related parts of the event topology, it is expected that some discriminating variables will be correlated. The method of Boosted Decision Trees is indeed sensitive to highly correlated variables and it may not be necessary to know the correlations when choosing the discriminant variables. However, it can be advantageous to reduce the variable list in order to simplify the trees by removing one of a set of highly correlated variables without a significant

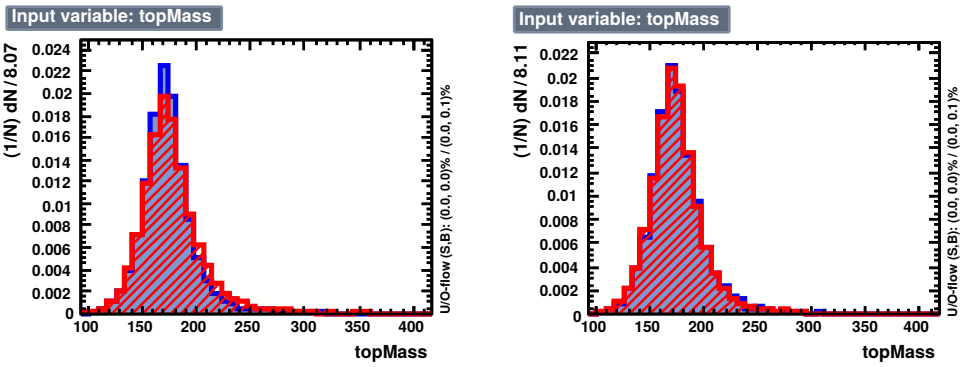

(A) 2J 2T category (B) 3J 2T category

FIGURE III.14: The reconstructed mass of the top quark.

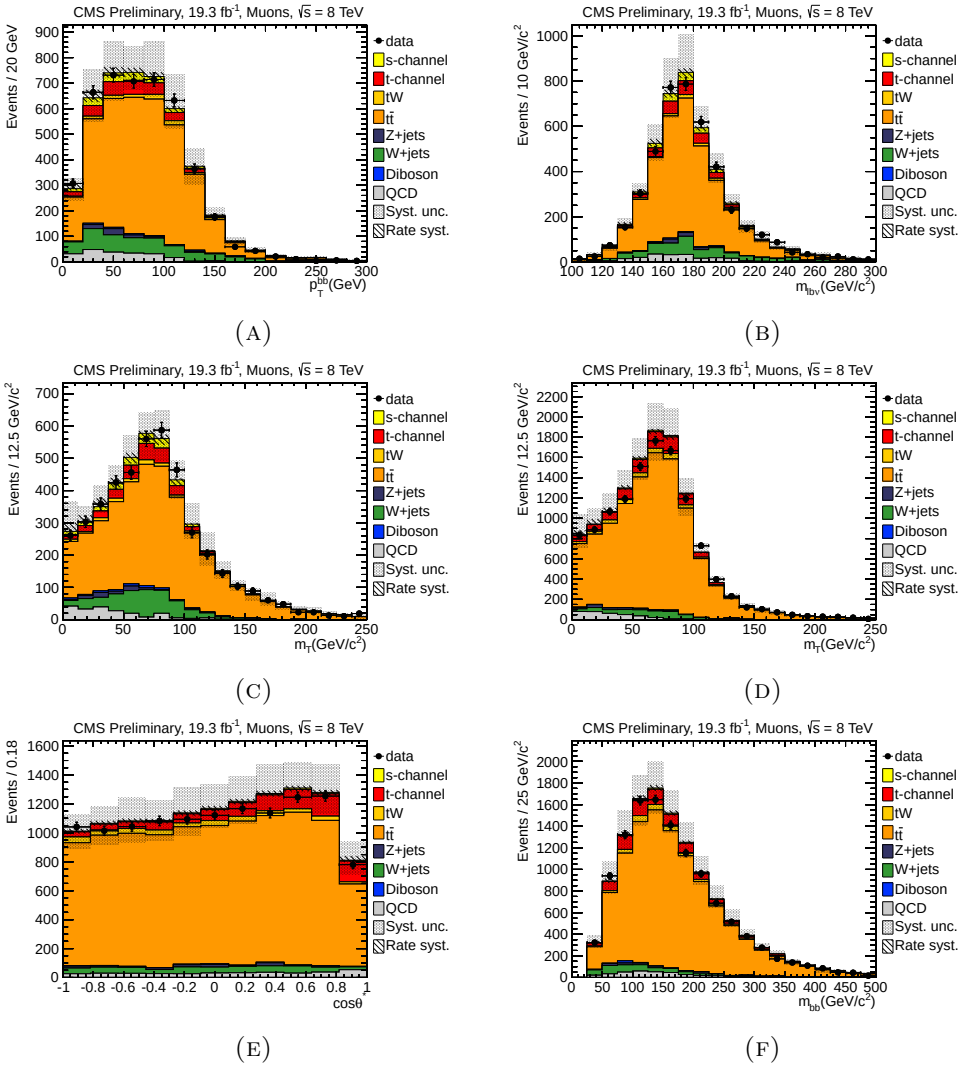

(A) (B) (C) (D) (E) (F)

FIGURE III.15: Distribution of some important variables for the 2J2T category including the systematic uncertainties.

loss in performance. This clearly advances the training time and reduces the number of variables one has to understand when dealing with systematic uncertainties and, of

course, the physical meaning of the output classifier. Therefore, a feedback mechanism was used to define a list of safe variables as described below.

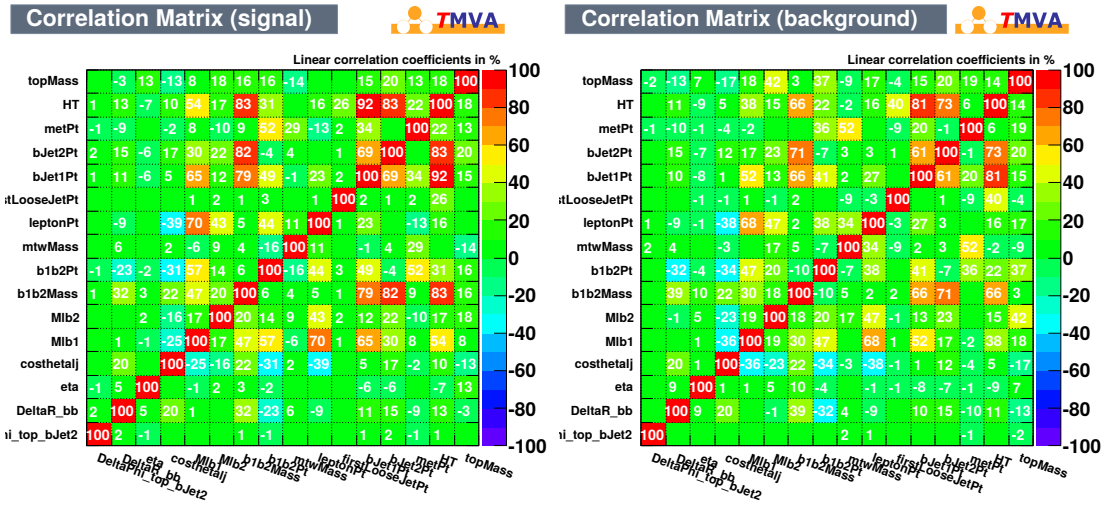

(A) 2J 2T category.

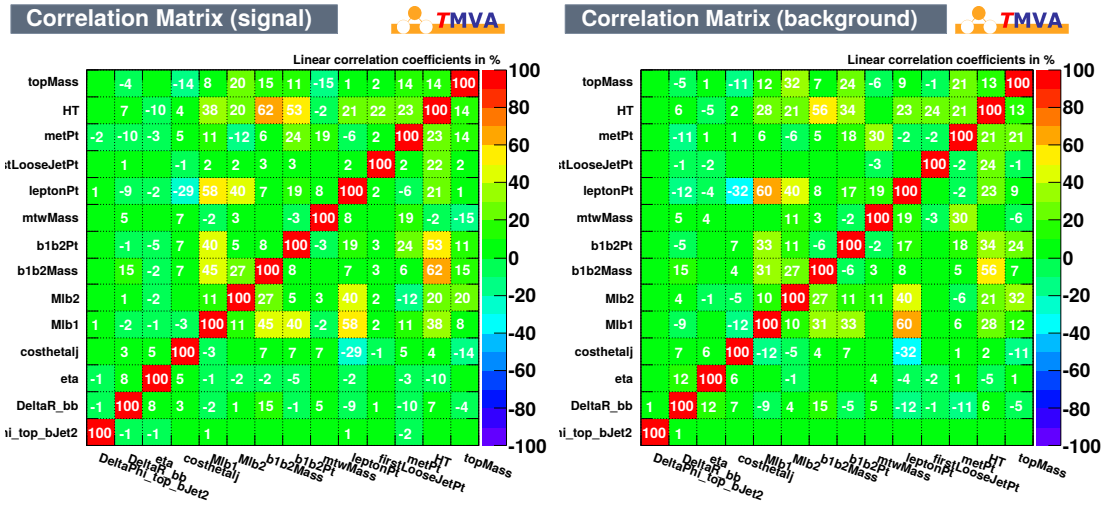

(B) 3J 2T category.

FIGURE III.16: Linear correlation coefficients.

In order to choose the most discriminating variables, it is used a mechanism that can compare iteratively the set of variables with each other with respect to their significance and correlation matrices. Starting with a set that is pursued to discriminate the signal would not always be the perfect case since some of the variables could discontribute to the BDT output by abbriviating the contributions of others.

The feedback loop used to end up with a safe list of variables simply compares the over-training, the signal/background seperation and the Receiver Operating Characteristic

(ROC) curve[1] integral for each variable list, iteratively, by removing the most correlated variable among the list. The loop is terminated when the significance of the signal-over-backround starts to decrease or the remaining variables have similar correlation coefficients.

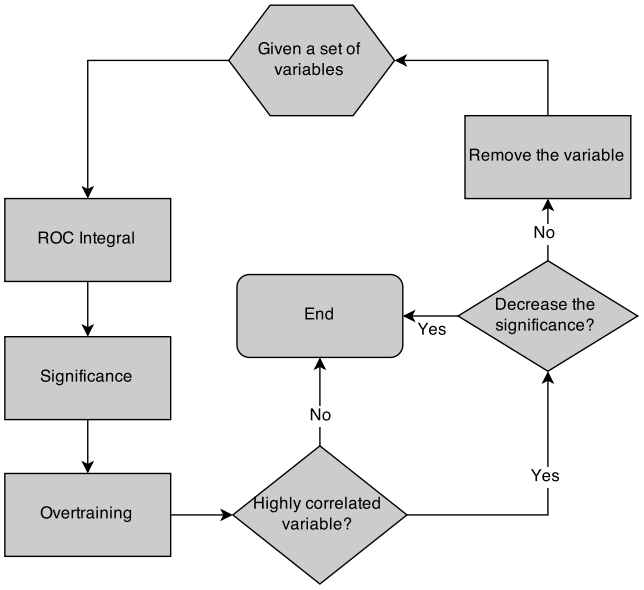

FIGURE III.17: The feedback loop

For each loop, a candidate variable is choosen according to its overall correlation with respect to the other variables in the correlation matrix. Explicitly, a variable is a removal candidate when the related row in the correlation matrix has the highest sum-of-squares value. The linear correlation coefficients are shown in Figure III.16 for the 2-jet 2-tagged and 3-jet 2-tagged categories. Therefore, if removing the candidate variable does not give a significant loss in the signal-background seperation, then it procedes to the next iteration by removing the candidate from the list until there are not any high overall correlation or the significance has decreased. This algorithm is described schematically in the Fig. III.17.

The feedback loops use only the correlations between the variables to choose a removal candidate. However, this work could be extended to be sensitive to as well as the

[1]Receiver Operating Characteristic curve illustrates the performance of a binary classifier system as its discrimination threshold is varied.

	Variable lists for 3J2T	Overtraining	ROC Int.
1	$\Delta\Phi_{tb'}$, ΔR_{bb}, η, $\cos\theta_{\ell j}$, M_{bb}, p_{T}^{bb}, m_{T}, $p_{\mathrm{T}}^{\mathrm{loose}}$, m_t, $\not\!\!E_{\mathrm{T}}$, p_{T}^{ℓ}, $M_{\ell b2}$, $M_{\ell b1}$, H_{T}	0.17 (0.31)	0.72
2	$\Delta\Phi_{tb'}$, ΔR_{bb}, η, $\cos\theta_{\ell j}$, M_{bb}, p_{T}^{bb}, m_{T}, $p_{\mathrm{T}}^{\mathrm{loose}}$, m_t, $\not\!\!E_{\mathrm{T}}$, p_{T}^{ℓ}, $M_{\ell b2}$, $M_{\ell b1}$	0.13 (0.71)	0.72
3	$\Delta\Phi_{tb'}$, ΔR_{bb}, η, $\cos\theta_{\ell j}$, M_{bb}, p_{T}^{bb}, m_{T}, $p_{\mathrm{T}}^{\mathrm{loose}}$, m_t, $\not\!\!E_{\mathrm{T}}$, p_{T}^{ℓ}, $M_{\ell b2}$	0.03 (0.89)	0.71
4	$\Delta\Phi_{tb'}$, ΔR_{bb}, η, $\cos\theta_{\ell j}$, M_{bb}, p_{T}^{bb}, m_{T}, $p_{\mathrm{T}}^{\mathrm{loose}}$, m_t, $\not\!\!E_{\mathrm{T}}$, p_{T}^{ℓ}	0.01 (0.75)	0.70
5	$\Delta\Phi_{tb'}$, ΔR_{bb}, η, $\cos\theta_{\ell j}$, M_{bb}, p_{T}^{bb}, m_{T}, $p_{\mathrm{T}}^{\mathrm{loose}}$, m_t, $\not\!\!E_{\mathrm{T}}$	0.07 (0.85)	0.70
6	$\Delta\Phi_{tb'}$, ΔR_{bb}, η, $\cos\theta_{\ell j}$, M_{bb}, p_{T}^{bb}, m_{T}, $p_{\mathrm{T}}^{\mathrm{loose}}$, m_t	0.01 (0.32)	0.70
7	$\Delta\Phi_{tb'}$, ΔR_{bb}, η, $\cos\theta_{\ell j}$, M_{bb}, p_{T}^{bb}, m_{T}, $p_{\mathrm{T}}^{\mathrm{loose}}$	0.02 (0.88)	0.70

TABLE III.2: The variable lists for the 3J 2T category, which are iterated via the feedback loop. The overtrainings are given as Kolmogorov-Smirnov tests between the test and the training samples for signal (background). Here, S and B denote signal and background events of the simulated data without systematic uncertainties, respectively.

systematic uncertainties since the deviation for each variable is large enough to change the behavior of the decision trees even if the correlation coefficients are exactly the same.

III.4.2 Training and Testing

The training of two independent Boosted Decision Trees is performed in the 2-jets 2-tags category to discriminate signal from the various background processes, and in the 3-jets 2-tags sample to separate $t\bar{t}$ from the rest. The goodness of the signal and background consistency is determined by the Kolmogorov-Smirnov test performed between the testing and the training parts of the samples, which are seperated randomly event by event from the simulated Monte Carlo data. It is expected that the control samples show very similar p-values after the iterations of the feedback machanism, at least above 0.01.

The significance, $S/\sqrt{S+B}$ where S is the number of signal events and B is the number of background events, is calculated according to the simulated data without taking into account the systematic uncertainties (See Table III.4).

The 2-jets 2-tags category had ten iterations, each shown in Table III.3 with its overtraining, ROC curve integral and significance, and their BDT output plotted in Figure

	Variable lists for 2J2T	Overtraining	ROC Int.	$S/\sqrt{S+B}$
1	$\Delta\Phi_{tb'}$, ΔR_{bb}, p_{T}^{b2}, p_{T}^{ℓ}, η, $p_{\mathrm{T}}^{\mathrm{loose}}$, $\not\!\!E_{\mathrm{T}}$, m_t, $\cos\theta_{\ell j}$, $M_{\ell b2}$, m_{T}, p_{T}^{bb}, p_{T}^{b1}, $M_{\ell b1}$, M_{bb}, H_{T}	0.31 (0.96)	0.80	2.2
2	$\Delta\Phi_{tb'}$, ΔR_{bb}, p_{T}^{b2}, p_{T}^{ℓ}, η, $p_{\mathrm{T}}^{\mathrm{loose}}$, $\not\!\!E_{\mathrm{T}}$, m_t, $\cos\theta_{\ell j}$, $M_{\ell b2}$, m_{T}, p_{T}^{bb}, p_{T}^{b1}, $M_{\ell b1}$, M_{bb}	0.47 (0.99)	0.79	2.2
3	$\Delta\Phi_{tb'}$, ΔR_{bb}, p_{T}^{b2}, p_{T}^{ℓ}, η, $p_{\mathrm{T}}^{\mathrm{loose}}$, $\not\!\!E_{\mathrm{T}}$, m_t, $\cos\theta_{\ell j}$, $M_{\ell b2}$, m_{T}, p_{T}^{bb}, p_{T}^{b1}, $M_{\ell b1}$	0.64 (0.95)	0.79	2.2
4	$\Delta\Phi_{tb'}$, ΔR_{bb}, p_{T}^{b2}, p_{T}^{ℓ}, η, $p_{\mathrm{T}}^{\mathrm{loose}}$, $\not\!\!E_{\mathrm{T}}$, m_t, $\cos\theta_{\ell j}$, $M_{\ell b2}$, m_{T}, p_{T}^{bb}, p_{T}^{b1}	0.72 (0.99)	0.79	2.2
5	$\Delta\Phi_{tb'}$, ΔR_{bb}, p_{T}^{b2}, p_{T}^{ℓ}, η, $p_{\mathrm{T}}^{\mathrm{loose}}$, $\not\!\!E_{\mathrm{T}}$, m_t, $\cos\theta_{\ell j}$, $M_{\ell b2}$, m_{T}, p_{T}^{bb}	0.50 (0.99)	0.79	2.2
6	$\Delta\Phi_{tb'}$, ΔR_{bb}, p_{T}^{b2}, p_{T}^{ℓ}, η, $p_{\mathrm{T}}^{\mathrm{loose}}$, $\not\!\!E_{\mathrm{T}}$, m_t, $\cos\theta_{\ell j}$, $M_{\ell b2}$, m_{T}	0.60 (0.99)	0.78	2.2
7	$\Delta\Phi_{tb'}$, ΔR_{bb}, p_{T}^{b2}, p_{T}^{ℓ}, η, $p_{\mathrm{T}}^{\mathrm{loose}}$, $\not\!\!E_{\mathrm{T}}$, m_t, $\cos\theta_{\ell j}$, $M_{\ell b2}$	0.40 (0.98)	0.77	2.1
8	$\Delta\Phi_{tb'}$, ΔR_{bb}, p_{T}^{b2}, p_{T}^{ℓ}, η, $p_{\mathrm{T}}^{\mathrm{loose}}$, $\not\!\!E_{\mathrm{T}}$, m_t, $\cos\theta_{\ell j}$	0.68 (0.90)	0.76	2.1
9	$\Delta\Phi_{tb'}$, ΔR_{bb}, p_{T}^{b2}, p_{T}^{ℓ}, η, $p_{\mathrm{T}}^{\mathrm{loose}}$, $\not\!\!E_{\mathrm{T}}$, m_t	0.88 (0.91)	0.76	2.1
10	$\Delta\Phi_{tb'}$, ΔR_{bb}, p_{T}^{b2}, p_{T}^{ℓ}, η, $p_{\mathrm{T}}^{\mathrm{loose}}$, $\not\!\!E_{\mathrm{T}}$	0.81 (0.89)	0.76	2.0

TABLE III.3: The variable lists for the 2J 2T category, which are iterated via the feedback loop. The overtrainings are given as Kolmogorov-Smirnov tests between the test and the training samples for signal (background). Here, S and B denote signal and background events of the simulated data without systematic uncertainties, respectively.

III.19. It turned out that the removed variable contributes insignificantly to the BDT output since the signal-over-background value has remained almost unchanged after ten iterations as well as the signal consistency stayed completely above the value of 1%. It can be seen that the seperation in the distribution has also been slightly improved comparing the first and the tenth iterations directly.

On the other hand, the 3-jets 2-tags category had seven iterations, as shown in Table III.2 with the overtraining and ROC curve integral. The BDT output of each iteration is plotted in Figure III.18. It could be seen that the seperation does not change while the most correlated variables were removed for each feedback loop.

The ROC curve, i.e., signal efficiency vs. background rejection remained without a significant change in both categories, 2-jets 2-tags and 3-jets 2-tags sample for each iteration.

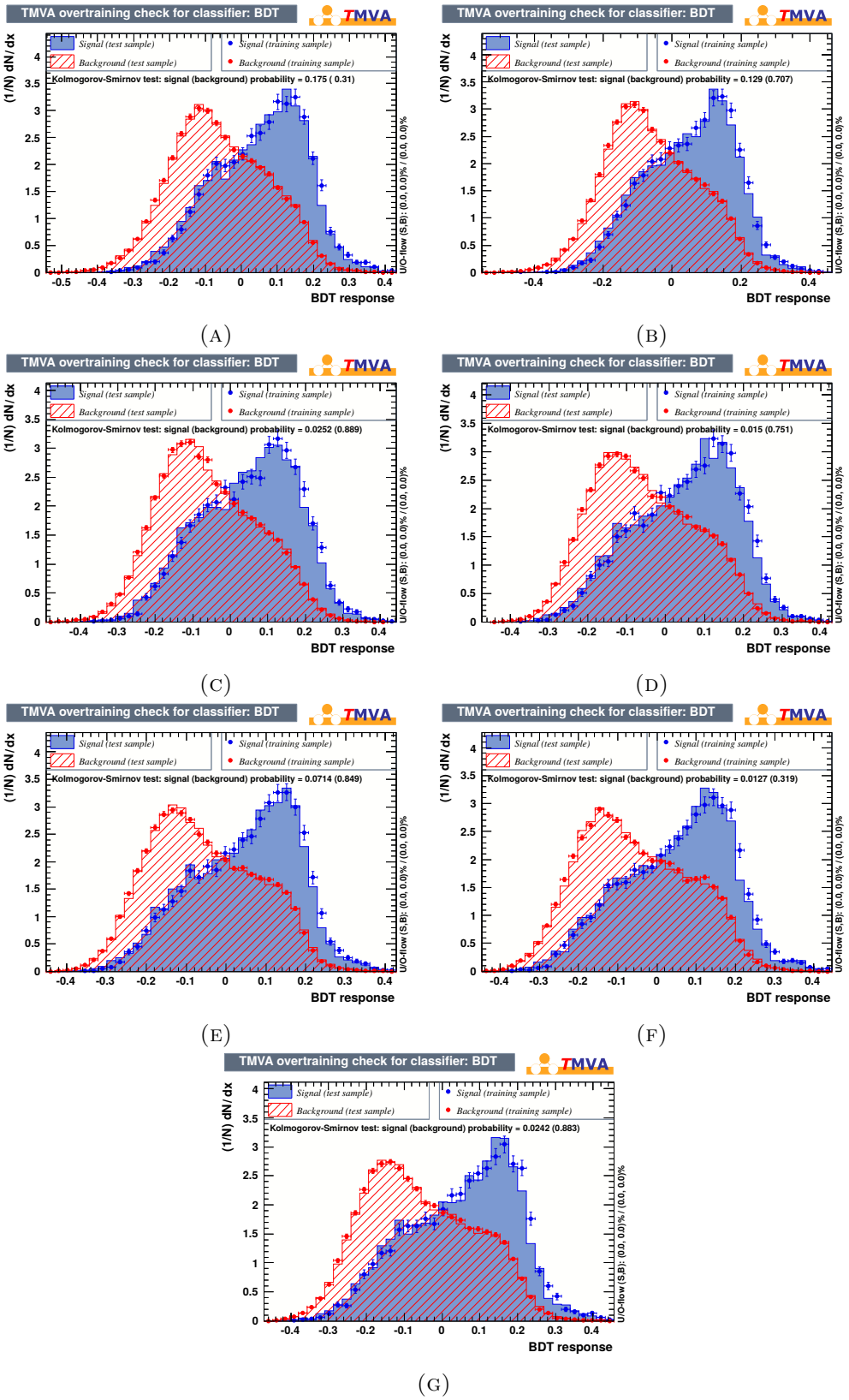

FIGURE III.18: The overtraining of the BDT output of each iteration in the feedback loop for the 3J2T category.

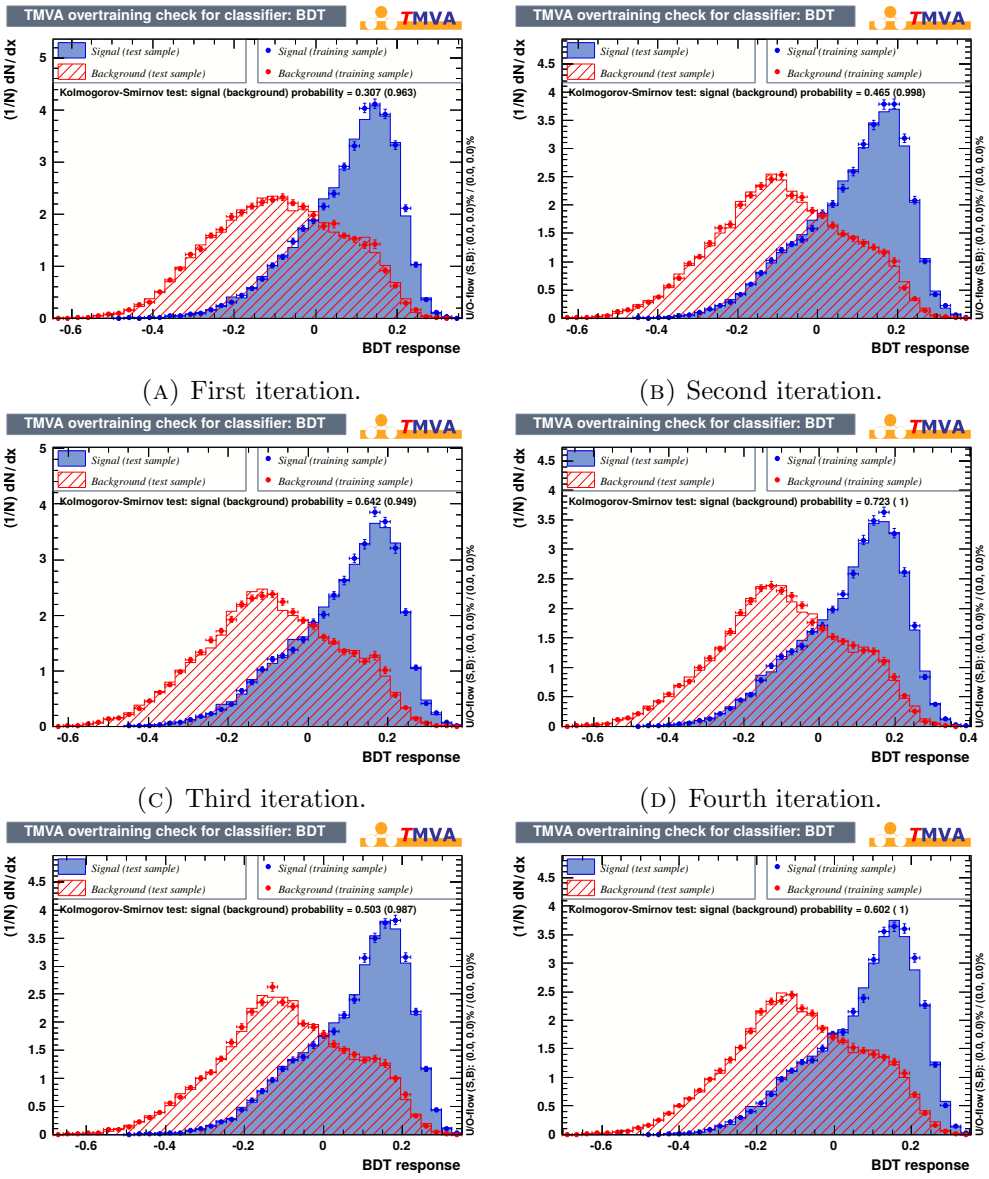

(A) First iteration. (B) Second iteration.

(C) Third iteration. (D) Fourth iteration.

(E) Fifth iteration. (F) sixth iteration.

FIGURE III.19: The overtraining of the BDT output of the first six iterations in the feedback loop for the 2J2T category.

The next natural step to be done in the future analyses is to perform a fit for the detector data with the BDT discriminant evaluated after the application of the feedback mechanism. In the next section, a previous measurement without the optimization of the feedback mechanism is presented.

III.4.3 Fit Procedure and the Measurement

The signal extraction is performed using the toolkit THETA [64]. It has been performed a binned maximum-likelihood fit to the BDT distributions on data in the 2-jets 2-tags

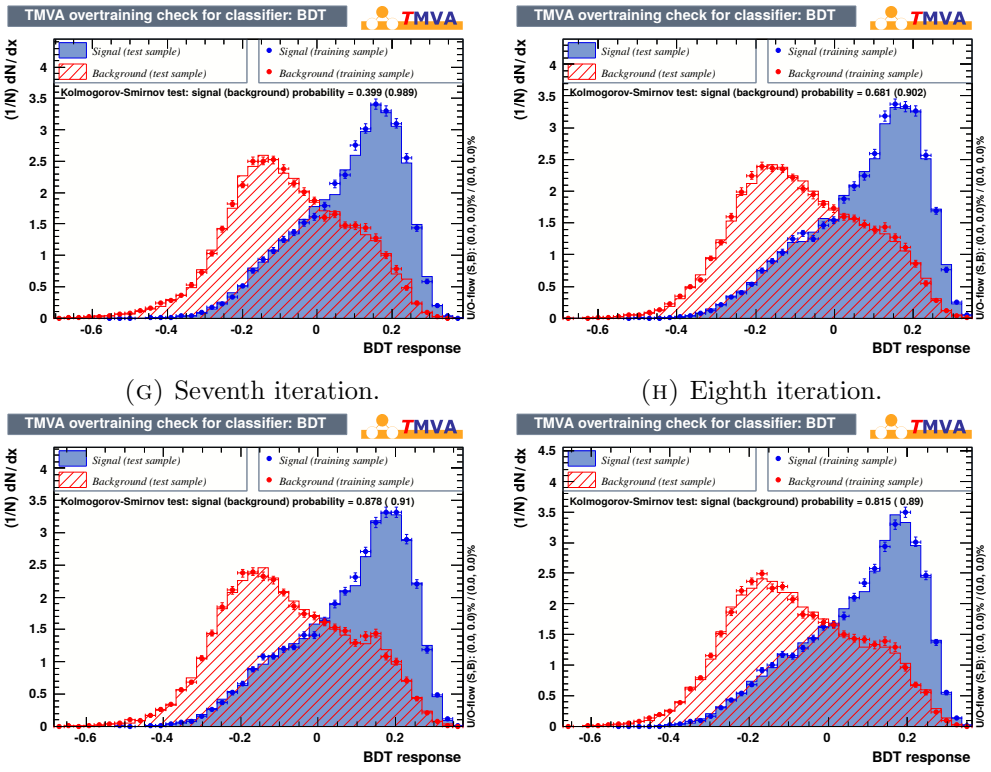

(G) Seventh iteration. (H) Eighth iteration.

(I) Ninth iteration. (J) Tenth iteration.

FIGURE III.19: The overtraining of the BDT output of last four iterations in the feedback loop for the 2J2T category.

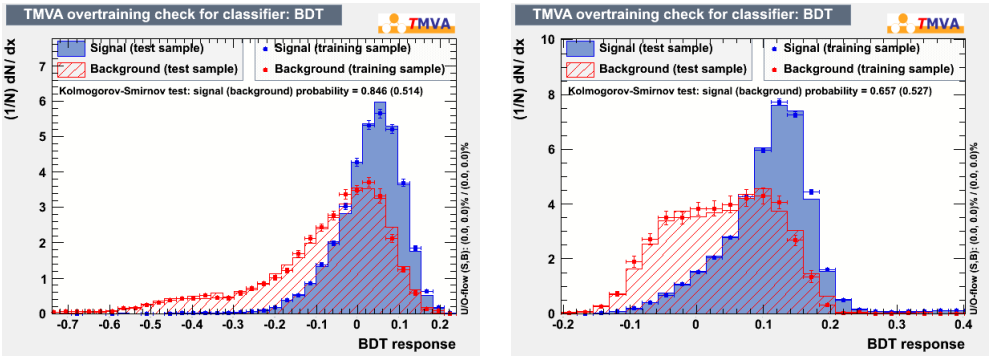

(A) 2J 2T category (B) 3J 2T category

FIGURE III.20: The overtraining of the BDT output from the analysis in [48].

and 3-jets 2-tags categories simultaneously. The expected total yield λ_i in each bin i of the BDT distribution is given by the sum of all the background contributions, plus the signal yield scaled by the signal strength modifier β_{signal} which is defined as the ratio between the measured signal cross section and the SM prediction, as follows:

$$\lambda_i(\beta_{\text{signal}}, \theta_u) = \beta_{\text{signal}} \cdot S_i(\theta_u) + \sum_p c_p(\theta_u) B_{p,i}(\theta_u) \tag{III.5}$$

where S and B_p are the models of BDT distributions, or shortly 'templates', for the s-channel and for each background process p, all scaled to the SM cross sections and to the dataset luminosity, c_p denotes the coefficient for the process template p, and θ_u is the nuisance parameter introduced to take into account the effect of each systematic uncertainty u on the measurement.

Systematic uncertainties affect the yield λ_i. The prior probability distribution for each nuisance parameter depends on the type of uncertainty. Background normalization uncertainties are modeled with a coefficient for the template B_p with a log-normal prior. Shape uncertainties are modeled by choosing a Gaussian prior for the nuisance parameter and performing an interpolation between the nominal template (which is not affected by θ_u) and the shifted templates obtained by applying $\pm 1\sigma$ systematic shift to the nominal one. The interpolation uses a smooth function which is cubic within 1σ range and uses a linear extrapolation beyond 1σ.

The 68% confidence interval for the parameter β_{signal} is evaluated from the excursion of the negative logarithm of the likelihood function around its minimum.

The likelihood model used for the signal extraction includes the background rates, luminosity and lepton efficiency nuisance parameters. The impact of individual systematic uncertainty on the s-channel cross-section measurement is evaluated removing one uncertainty at a time from the likelihood model and measuring the corresponding variation in the profile likelihood.

The other instrumental and theoretical uncertainties, whose inclusion in the likelihood model leads to fit instabilities, are evaluated with the following procedure. Two pseudodatasets are generatd in which the nuisance parameter in interest is set to $\pm 1\sigma$ with respect to its nominal value and the other are fixed to zero. Two maximum-likelihood fits are performed for the $+1\sigma$ and -1σ variations separately and the differences between the fitted β_{signal} and one (nominal value used in pseudodatasets generation) are taken as the corresponding uncertainties.

The sensivity to the s-channel single-top signal has been evaluated using the derivative of the likelihood test statistics. It is defined as in the following:

$$q_0 = \frac{\partial}{\partial \beta_{signal}} \log L \Big|_{\beta_{signal}=0} \tag{III.6}$$

which is evaluated at the maximum likelihood estimate of the background-only hypothesis. Pseudoexperiments are diced and the distribution of the test statistics is obtained for the background-only and the signal-plus-background hypotheses. The median of the distribution in the signal-plus-background hypothesis represents the expected significance of the measurement. The observed significance is measured from the tail of the q_0 distribution in the background-only hypothesis after evaluating the test statistics on data.

Uncertainty source (%)	Muons
stat. uncertainty	±33
W/Z+jets, diboson rate	±20
QCD rate	±19
JER+JES	±83
unclustered $\not\!\!E_{\mathrm{T}}$	±49
Q^2	±64
matching thresholds	±41
rest	±31
total uncertainty	±145

TABLE III.4: Summary of the relative impact of each systematic uncertainty on the cross-section measurement. The item, "rest", includes the following sources: PDF, top mass, mis-tag, pile-up, b-tagging, lepton SF, luminosity, $t\bar{t}$ rate and single-top rate.

The single-top s-channel inclusive production cross section has been measured without using the feedback mechanism, in [48], as a 68% confidence level (CL) interval using the Feldman-Cousins unified approach, to be as the following:

$$\sigma_{s\text{-ch.}} \quad = \quad 5.9^{+8.6}_{-5.1} \text{ pb} \quad \text{muon channel}$$

and it has become $\sigma_{s\text{-ch.}} = 6.2^{+8.0}_{-5.1}$ pb when combined with the electron channel. The impact of the systematic uncertainties on the measurement is summarized in Table III.4.

The observed and expected upper limits, the latter denoted as "(SM signal, background-only)", on the s-channel cross section using the CL_s method are evaluated, as well. The upper limit at 95% CL is 2.2 (3.3, 1.9) times the SM cross section, which corresponds to 12.4 (18.4, 10.5) pb, in the muon channel. In the electron channel, the upper limit at 95% CL is 2.6 (4.2, 2.8) times the SM cross section, which corresponds to 14.7 (23.2, 15.4) pb. Combining the two channels we obtain an upper limit of 2.1 (3.1, 1.6) times the SM cross section corresponding to 11.5 (17.0, 9.0) pb.

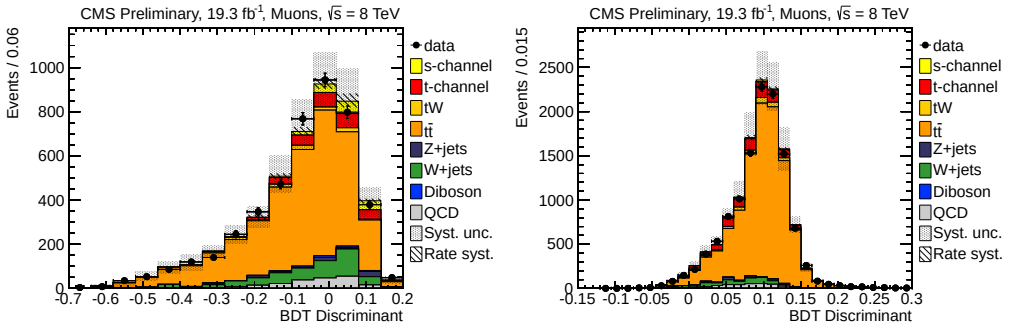

(A) 2J2T category (B) 3J2T category

FIGURE III.21: The BDT output of the fitted data.

It is expected that using the iterative optimization of the variables for the signal and control samples would also improve the measurement of the cross-section. In a future study, the sensivity of the variables to the systematic uncertainties could be taken into account in the feedback loop, as well.

III.5 Results

The analysis is performed using a multivariate technique called Boosted Decision Trees which takes a list of variables as input and a discriminant variable, which is obtained by testing and training of a learning algorithm, as output. The output variable is used to discriminate the signal, which is the events of single top-quark production in the *s*-channel, from the background which consist of various processes dominated by $t\bar{t}$ events.

The choice of the input variables is optimized using a feedback loop over each iteration removing a single variable that has the most overall correlation among other variables for the signal. The loop ends when there is a significant decrease in the signal-background separation.

The optimization procedure manifests that it can be used less variables to discriminate the signal from the background. The feedback loop provides a statistical procedure that is manifesting a global and holistic approach to the BDT analysis, instead of considering a variable of the process individually. This gives a possibility to understand the physics behind the correlations of the variables with respect to their discrimination power for the topology in subject.

Conclusion

A multivariate study based on Boosted Decision Trees has been performed for the search of single top-quark production with muonic final state topology in s-channel with a center-of-mass energy of 8 TeV in the CMS experiment at CERN. The BDT output is obtained by optimizing the choice of the input variables by iterating in a feedback loop globally sensitive to the correlation coefficients of the variables. Then, the optimized BDT discriminant is compared with the analysis which was performed without any optimization on the choice of inputs.

It has been investigated that the BDT output does not reveal any significant change in the separating power as the most globally correlated variables are removed, iteratively. Therefore, reducing the variable list in this way can be advantageous since it advances our understanding for the physical meaning of the output classifier. In the study, it is also stressed that the systematic uncertainties are not included in the optimization however the feedback mechanism can be naturally extended to a such feature.

As a result, the feedback mechanism clearly provides different optimizations for different event topologies in the fact that the variables are taken into account in a holistic approach, by looking at the overall correlations among the variables, instead of a choice made on the individual properties of the variables. This study is a first consideration for the optimization of the BDT analyses in the single top-quark production.

As a next step, this results will be used to fit the data accounting the systematic uncertainties and extract the cross-section for the BDT discriminant obtained by this study.

Acknowledgements

First, I would like to thank my insightful and warm supervisor Dr. Luca Lista for the opportunity of working with him in the "Single Top" group in Naples, and as well as Dr. Mario Merola for collaborating and supervising very wisely and closely during my work.

I feel very grateful to Prof. Raffaele Velotta for his kind and sincere relationship with me during my Ph.D.

My gratitudes to Prof. Fabio Ambrosino and Prof. Guglielmo De Nardo for their useful and wise comments, both in the Ph.D workshop and in personal discussions.

I should surely give my special thanks to my good friends in the Ph.D room for their warm, friendly and, most of the times, fun atmosphere. I would like to thank also Guido Celentano for his helps and especially his friendly and cheerful behaviour. My parents and my brother deserve a special thank for their live spiritual support from far-off Turkey.

Finally, I would like to give my endless love and thanks to my joyful and endearious wife Asuman for devoted efforts, deep wisdom and everlasting love. Without her, it would be impossible achieve up to the present.

List of Figures

I.1 The single top-quark production in s-channel (left), W-associated t-channel (middle) and t-channel (right). . . . 22

II.1 The total integrated luminosity recorded by the CMS experiment in 2010, 2011 and 2012. . . . 27
II.2 The LHC injection complex. . . . 27
II.3 The LHC layout. . . . 29
II.4 The LHC dipole cross-section [52]. . . . 30
II.5 The design of the Compact Muon Selenoid. . . . 34
II.6 The tracker system. . . . 35
II.7 The hadron calorimeter (HCAL). ECAL and trackers also appear at the innermost part. . . . 35
II.8 The hadronic calorimeter (HCAL). . . . 36
II.9 The muon system of the CMS detector. . . . 37

III.1 Transverse mass of the W boson in 2J2T category for the muon channel. . 53
III.2 Transverse mass of the W boson for the muon channel. . . . 57
III.3 The difference in azimuthal angle between top quark and recoiled b-tagged jet for the muon channel. . . . 58
III.4 Transverse momentum of the muon channel. . . . 58
III.5 Missing transverse energy for the muon channel. . . . 59
III.6 Invariant mass of the lepton and the second-to-leading b-tagged jet. . . . 59
III.7 Invariant mass of the lepton and the second-to-leading b-tagged jet. . . . 59
III.8 Cosine of the angle between the lepton and the b-tagged jet recoiling against the top quark. . . . 60
III.9 Vector sum of p_T of the two b-tagged jets. . . . 60
III.10 The angular separation between the b-tagged jet recoiling against the top quark and the lepton. . . . 61
III.11 Scalar sum of p_T of all jets. . . . 62
III.12 The pseudorapidity. . . . 62
III.13 Invariant mass of the leading and the second-to-leading b-tagged jet. . . . 62
III.14 The reconstructed mass of the top quark. . . . 63
III.15 Distribution of some important variables for the 2J2T category including the systematic uncertainties. . . . 63
III.16 Linear correlation coefficients. . . . 64
III.17 The feedback loop 65
III.18 The overtraining of the BDT output of each iteration in the feedback loop for the 3J2T category. . . . 68

III.19The overtraining of the BDT output of the first six iterations in the feedback loop for the 2J2T category. 69
III.19The overtraining of the BDT output of last four iterations in the feedback loop for the 2J2T category. 70
III.20The overtraining of the BDT output from the analysis in [48]. 70
III.21The BDT output of the fitted data. 73

List of Tables

I.1 The periodic table of Standard Model. The anti-particles are not included. 8
I.2 Table of the Standard Model predictions for the top-pair production cross-sections at NNLO with NNNLL self-gluon corrections [21]. 21
I.3 Table of the Standard Model predictions for the single top production cross-sections for all three production channels at NNLO [22–26]. 22

III.1 The options used for the BDT method in this analysis. 56
III.2 The variable lists for the 3J 2T category, which are iterated via the feedback loop. The overtrainings are given as Kolmogorov-Smirnov tests between the test and the training samples for signal (background). Here, S and B denote signal and background events of the simulated data without systematic uncertainties, respectively. 66
III.3 The variable lists for the 2J 2T category, which are iterated via the feedback loop. The overtrainings are given as Kolmogorov-Smirnov tests between the test and the training samples for signal (background). Here, S and B denote signal and background events of the simulated data without systematic uncertainties, respectively. 67
III.4 Summary of the relative impact of each systematic uncertainty on the cross-section measurement. The item, "rest", includes the following sources: PDF, top mass, mis-tag, pile-up, b-tagging, lepton SF, luminosity, $t\bar{t}$ rate and single-top rate. 72

Bibliography

[1] J. Beringer et al. Review of Particle Physics (RPP). *Phys.Rev.*, D86:010001, 2012. doi: 10.1103/PhysRevD.86.010001. SLAC-REPRINT-2014-001.

[2] D. Griffiths. *Introduction to Elementary Particles.* John Wiley & Sons, New York, USA, 1987.

[3] S. L. Glashow. Partial symmetries of weak interactions. *Nucl. Phys.*, 22:579–588, 1961.

[4] S. Weinberg. A model of leptons. *Phys. Rev. Lett.*, 19:1264–1266, 1967.

[5] A. Salam. Weak and electromagnetic interactions. 1969. Proc. of the 8th Nobel Symposium on 'Elementary particle theory, relativistic groups and analyticity', Stockholm, Sweden, 1968, edited by N. Svartholm, p.367-377.

[6] Steven Weinberg. Effects of a neutral intermediate boson in semileptonic processes. *Phys. Rev.*, D5:1412–1417, 1972.

[7] Elliot Leader and Enrico Predazzi. *An Introduction to Gauge Theories and Modern Particle Physics.* Cambridge monographs on particle physics, nuclear physics, and cosmology. Cambridge Univ. Press, Cambridge, 1996.

[8] Ian J R Aitchison and Anthony J G Hey. *Gauge theories in particle physics: a practical introduction; 4th ed.* CRC Press, Boca Raton, FL, 2013.

[9] Peter W. Higgs. Broken symmetries, massless particles and gauge fields. *Phys. Lett.*, 12:132–133, 1964.

[10] Peter W. Higgs. Spontaneous symmetry breakdown without massless bosons. *Phys. Rev.*, 145:1156–1163, 1966.

[11] F. Englert and R. Brout. Broken symmetry and the mass of gauge vector mesons. *Phys. Rev. Lett.*, 13:321–322, 1964.

[12] G. S. Guralnik, C. R. Hagen, and T. W. B. Kibble. Global conservation laws and massless particles. *Phys. Rev. Lett.*, 13:585–587, 1964.

[13] P. A. M. Dirac. The quantum theory of dispersion. 114(769):710–728, May 1927. ISSN 0080-4630.

[14] P. Jordan and W. Pauli, Jr. Zur Quantenelektrodynamik ladungsfreier Felder. (German) [On quantum electrodynamics of charge-free fields]. 47(3–4):151–173, February 1928. ISSN 0939-7922 (print), 1431-5831 (electronic). doi: http://dx.doi.org/10.1007/BF02055793.

[15] W. Heisenberg and W. Pauli. Zur Quantendynamik der Wellenfelder. (German) [On the quantum dynamics of wave fields]. 56(1–2):1–61, January 1929. ISSN 0939-7922 (print), 1431-5831 (electronic). doi: http://dx.doi.org/10.1007/BF01340129.

[16] Julian Schwinger. On quantum-electrodynamics and the magnetic moment of the electron. *Phys. Rev.*, 73(4):416–417, February 1948. doi: 10.1103/PhysRev.73.416.

[17] R. P. Feynman. The theory of positrons. 76(6):749–759, September 1949. ISSN 0031-899X (print), 1536-6065 (electronic). doi: http://dx.doi.org/10.1103/PhysRev.76.749.

[18] Michael E. Peskin and Daniel V. Schroeder. An Introduction to quantum field theory. 1995. ISBN-9780201503975.

[19] N. Cabibbo. Unitary symmetry and leptonic decays. *Phys. Rev. Lett.*, 10:531–532, 1963.

[20] M. Kobayashi and T. Maskawa. Cp violation in the renormalizable theory of weak interaction. *Prog. Theor. Phys.*, 49:652–657, 1973.

[21] Nikolaos Kidonakis. NNNLO soft-gluon corrections for the top-antitop pair production cross section. *Phys.Rev.*, D90(1):014006, 2014. doi: 10.1103/PhysRevD.90.014006.

[22] M. Assadsolimani, P. Kant, B. Tausk, and P. Uwer. Calculation of two-loop QCD corrections for hadronic single top-quark production in the t channel. *Phys.Rev.*, D90(11):114024, 2014. doi: 10.1103/PhysRevD.90.114024. HU-EP-14-32, SFB-CPP-14-71.

[23] Nikolaos Kidonakis. NNLL threshold resummation for top-pair and single-top production. *Phys.Part.Nucl.*, 45(4):714–722, 2014. doi: 10.1134/S1063779614040091.

[24] Nikolaos Kidonakis. Next-to-next-to-leading-order collinear and soft gluon corrections for t-channel single top quark production. *Phys.Rev.*, D83:091503, 2011. doi: 10.1103/PhysRevD.83.091503.

[25] Nikolaos Kidonakis. Two-loop soft anomalous dimensions for single top quark associated production with a W- or H-. *Phys.Rev.*, D82:054018, 2010. doi: 10.1103/PhysRevD.82.054018.

[26] Nikolaos Kidonakis. NNLL resummation for s-channel single top quark production. *Phys.Rev.*, D81:054028, 2010. doi: 10.1103/PhysRevD.81.054028.

[27] T. Aaltonen et al. First Observation of Electroweak Single Top Quark Production. *Phys.Rev.Lett.*, 103:092002, 2009. doi: 10.1103/PhysRevLett.103.092002. FERMILAB-PUB-09-059-E.

[28] T. Aaltonen et al. Measurements of the top-quark mass using charged particle tracking. *Phys.Rev.*, D81:032002, 2010. doi: 10.1103/PhysRevD.81.032002. FERMILAB-PUB-09-464-E.

[29] T. Aaltonen et al. Observation of Single Top Quark Production and Measurement of —Vtb— with CDF. *Phys.Rev.*, D82:112005, 2010. doi: 10.1103/PhysRevD.82.112005. FERMILAB-PUB-10-063-E.

[30] V.M. Abazov et al. Observation of Single Top Quark Production. *Phys.Rev.Lett.*, 103:092001, 2009. doi: 10.1103/PhysRevLett.103.092001. FERMILAB-PUB-09-056-E.

[31] Victor Mukhamedovich Abazov et al. Measurements of single top quark production cross sections and $|V_{tb}|$ in $p\bar{p}$ collisions at $\sqrt{s} = 1.96$ TeV. *Phys.Rev.*, D84:112001, 2011. doi: 10.1103/PhysRevD.84.112001. FERMILAB-PUB-11-380-E.

[32] Timo Antero Aaltonen et al. Measurement of the Single Top Quark Production Cross Section and $|V_{tb}|$ in Events with One Charged Lepton, Large Missing Transverse Energy, and Jets at CDF. *Phys.Rev.Lett.*, 113(26):261804, 2014. doi: 10.1103/PhysRevLett.113.261804. FERMILAB-PUB-14-229-E.

[33] Timo Antero Aaltonen et al. Updated Measurement of the Single Top Quark Production Cross Section and Vtb in the Missing Transverse Energy Plus Jets Topology in $p\bar{p}$ Collisions at $\sqrt{s} = 1.96$ TeV. 2014. FERMILAB-PUB-14-398-E.

[34] Victor Mukhamedovich Abazov et al. Evidence for s-channel single top quark production in $p\bar{p}$ collisions at $\sqrt{s} = 1.96$ TeV. *Phys.Lett.*, B726:656–664, 2013. doi: 10.1016/j.physletb.2013.09.048. FERMILAB-PUB-13-252-E.

[35] Victor Mukhamedovich Abazov et al. Model-independent measurement of t-channel single top quark production in $p\bar{p}$ collisions at $\sqrt{s} = 1.96$ TeV. *Phys.Lett.*, B705:313–319, 2011. doi: 10.1016/j.physletb.2011.10.035. FERMILAB-PUB-11-216-E.

[36] Timo Antero Aaltonen et al. Evidence for s-channel Single-Top-Quark Production in Events with one Charged Lepton and two Jets at CDF. *Phys.Rev.Lett.*, 112: 231804, 2014. doi: 10.1103/PhysRevLett.112.231804. FERMILAB-PUB-14-015-E.

[37] Timo Antero Aaltonen et al. Search for s-Channel Single-Top-Quark Production in Events with Missing Energy Plus Jets in $p\bar{p}$ Collisions at $\sqrt{s}$ =1.96 TeV. *Phys.Rev.Lett.*, 112(23):231805, 2014. doi: 10.1103/PhysRevLett.112.231805. FERMILAB-PUB-14-027-E.

[38] Timo Antero Aaltonen et al. Observation of s-channel production of single top quarks at the Tevatron. *Phys.Rev.Lett.*, 112:231803, 2014. doi: 10.1103/PhysRevLett.112.231803. FERMILAB-PUB-14-031-E.

[39] Georges Aad et al. Measurement of the t-channel single top-quark production cross section in pp collisions at $\sqrt{s} = 7$ TeV with the ATLAS detector. *Phys.Lett.*, B717: 330–350, 2012. doi: 10.1016/j.physletb.2012.09.031. CERN-PH-EP-2012-082.

[40] Georges Aad et al. Comprehensive measurements of t-channel single top-quark production cross sections at $\sqrt{s} = 7$ TeV with the ATLAS detector. *Phys.Rev.*, D90 (11):112006, 2014. doi: 10.1103/PhysRevD.90.112006. CERN-PH-EP-2014-133.

[41] Serguei Chatrchyan et al. Measurement of the t-channel single top quark production cross section in pp collisions at $\sqrt{s} = 7$ TeV. *Phys.Rev.Lett.*, 107:091802, 2011. doi: 10.1103/PhysRevLett.107.091802. CERN-PH-EP-2011-066, CMS-TOP-10-008.

[42] Georges Aad et al. Measurement of t-Channel Single Top-Quark Production in pp Collisions at sqrt(s) = 8 TeV with the ATLAS detector. Technical report, 2012. ATLAS-CONF-2012-132, ATLAS-COM-CONF-2012-169.

[43] CMS Collaboration. Measurement of the single-top t-channel cross section in pp collisions at centre-of-mass energy of 8 TeV. Technical report, 2012. CMS-PAS-TOP-12-011.

[44] Georges Aad et al. Evidence for the associated production of a W boson and a top quark in ATLAS at $\sqrt{s} = 7$ TeV. *Phys.Lett.*, B716:142–159, 2012. doi: 10.1016/j.physletb.2012.08.011. CERN-PH-EP-2012-117.

[45] Serguei Chatrchyan et al. Observation of the associated production of a single top quark and a W boson in pp collisions at $\sqrt{s}$ =8 TeV. *Phys.Rev.Lett.*, 112(23): 231802, 2014. doi: 10.1103/PhysRevLett.112.231802. CMS-TOP-12-040, CERN-PH-EP-2013-237.

[46] Serguei Chatrchyan et al. Evidence for associated production of a single top quark and W boson in pp collisions at $\sqrt{s} = 7$ TeV. *Phys.Rev.Lett.*, 110:022003, 2013. doi: 10.1103/PhysRevLett.110.022003. CMS-TOP-11-022, CERN-PH-EP-2012-266.

[47] Georges Aad et al. Search for s-channel single top-quark production in proton–proton collisions at $\sqrt{s} = 8$ TeV with the ATLAS detector. *Phys.Lett.*, B740: 118–136, 2015. doi: 10.1016/j.physletb.2014.11.042. CERN-PH-EP-2014-224.

[48] CMS Collaboration. Measurement of the single top s-channel cross section at 8 TeV. Technical report, 2013. CMS-PAS-TOP-13-009.

[49] Vardan Khachatryan et al. Measurement of the t-channel single-top-quark production cross section and of the $| V_{tb} |$ CKM matrix element in pp collisions at $\sqrt{s}$= 8 TeV. *JHEP*, 1406:090, 2014. doi: 10.1007/JHEP06(2014)090. CMS-TOP-12-038, CERN-PH-EP-2014-032.

[50] Oliver Sim Brüning, Paul Collier, P Lebrun, Stephen Myers, Ranko Ostojic, John Poole, and Paul Proudlock. *LHC Design Report*. CERN, Geneva, 2004.

[51] Michael Benedikt, Paul Collier, V Mertens, John Poole, and Karlheinz Schindl. *LHC Design Report*. CERN, Geneva, 2004.

[52] Jean-Luc Caron. Cross section of LHC dipole.. Dipole LHC: coupe transversale. AC Collection. Legacy of AC. Pictures from 1992 to 2002., May 1998.

[53] *CMS, the Compact Muon Solenoid: technical proposal*. LHC Tech. Proposal. CERN, Geneva, 1994. Cover title : CMS, the Compact Muon Solenoid : technical proposal.

[54] *CMS TriDAS project: Technical Design Report, Volume 1: The Trigger Systems*. Technical Design Report CMS.

[55] *The CMS electromagnetic calorimeter project: Technical Design Report*. Technical Design Report CMS. CERN, Geneva, 1997.

[56] *The CMS hadron calorimeter project: Technical Design Report*. Technical Design Report CMS. CERN, Geneva, 1997.

[57] Particle-Flow Event Reconstruction in CMS and Performance for Jets, Taus, and MET. Technical Report CMS-PAS-PFT-09-001, CERN, 2009. Geneva, Apr 2009.

[58] Wolfgang Adam, Boris Mangano, Thomas Speer, and Teddy Todorov. Track Reconstruction in the CMS tracker. Technical Report CMS-NOTE-2006-041, CERN, Geneva, Dec 2006.

[59] Andrea Rizzi, Fabrizio Palla, and Gabriele Segneri. Track impact parameter based b-tagging with CMS. Technical Report CMS-NOTE-2006-019, CERN, Geneva, Jan 2006.

[60] Matteo Cacciari, Gavin P. Salam, and Gregory Soyez. The Anti-k(t) jet clustering algorithm. *JHEP*, 0804:063, 2008. doi: 10.1088/1126-6708/2008/04/063. LPTHE-07-03.

[61] CMS Collaboration. b-Jet Identification in the CMS Experiment. 2012. CMS-PAS-BTV-11-004.

[62] M.R. Whalley, D. Bourilkov, and R.C. Group. The Les Houches accord PDFs (LHAPDF) and LHAGLUE. 2005.

[63] Andreas Hocker, J. Stelzer, F. Tegenfeldt, H. Voss, K. Voss, et al. TMVA - Toolkit for Multivariate Data Analysis. *PoS*, ACAT:040, 2007. CERN-OPEN-2007-007.

[64] T. Muller, J. Ott, and J. Wagner-Kuhr. THETA - A framework for template-based modeling and inference, 2010. CERN-IN-2010-017.